Physiological and Data-Driven Modeling for Time Series Prediction of Motion Sickness Using Multiple Sensory Inputs

by

Daniel Sousa Schulman

A dissertation submitted in partial fulfillment
of the requirements for the degree of
Doctor of Philosophy
(Mechanical Engineering)
in the University of Michigan
2025

Doctoral Committee:

Professor Shorya Awtar, Chair
Professor Xun Huan
Associate Research Scientist Dr. Monica Jones
Professor Bernard Martin

Daniel Sousa Schulman
dschul@umich.edu
ORCID iD: 0000-0003-2001-4904

© Daniel Sousa Schulman 2025

DEDICATION

To my mom, Rosane, and my grandma, Dirce, for providing incredible support since my early years.
To my dad, Philippe, and my sister, Debora, for all their care and love.
To my wife, Alicia, for being my rock and believing in me.
To all my friends and family for the unconditional love and support.
In memory of my friend, Fawaz Ali, whose support and dedication inspired me throughout the past years.

Obrigado!

ACKNOWLEDGEMENTS

I'd like to thank Prof. Shorya Awtar for the invaluable guidance throughout these past years. Your mentorship is greatly appreciated, and it has taught me invaluable lessons that have made me not only a better engineer but also a better human. It's been an honor to work with you, and I'm excited about the ventures ahead.

I'd like to thank the doctoral thesis committee for the invaluable advice and guidance. Dr. Monica Jones, your work with motion sickness was a precursor to much covered in this thesis, and this work would not be possible without your shoulders to stand on. I appreciate your guidance and your unwavering collaboration. Prof. Martin, thank you for the valuable insights into the experimental work that led to the dataset used for much of this work. Prof. Huan, your work has been heavily inspiring to me and helped me realize the capabilities of machine learning models in mechanical engineering.

I would also like to thank the incredible team of engineers at the Precision Systems Design Lab for making this work possible. You made major contributions to the work described in this thesis. In particular, thank you to Nishant Jalgaonkar, Bradley Kerr, Srikanth Kodandaramaiah, and Siyuan Yin for all the hard work!

Thank you to our sponsors at the Center for Connected and Automated Transportation (CCAT), the Michigan Translational Research and Commercialization (MTRAC) Hub, and to our collaborators at Mcity for the support throughout all these years and for believing in this project.

TABLE OF CONTENTS

DEDICATION ii

ACKNOWLEDGEMENTS iii

LIST OF FIGURES vi

LIST OF TABLES viii

ABSTRACT x

CHAPTER

1 Introduction and Background 1

2 Literature Review and Gaps in Current Research 8

2.1 Physiological Models for Motion Sickness 8
2.2 Data-Driven Models for Motion Sickness 14

3 A Visual-Vestibular Model to Predict Motion Sickness for Linear and Angular Motion 18

3.1 Proposed Model 18
3.2 Results and Discussion 24
3.3 Conclusion & Future Work 33

4 Experimental Protocol for Collection of On-Road Motion Sickness Data when Passengers Are Performing Tasks and Exposed to Preemptive Haptic Stimuli 35

5 Data-Driven Prediction of Car Sickness Using Head Motion and Time Series Feature Engineering Methods 43

5.1 Data Preprocessing 43
5.2 Predictive Modeling 50
5.2.1 Regression 50
5.2.2 Classification 54
5.3 Results 61
5.4 Discussion 63
5.5 Conclusion & Future Work 66

6 Physiological Data-Driven Models for Motion Sickness Prediction 68
6.1 Data Preprocessing 69
6.2 Predictive Modeling 70
6.3 Results 88
6.4 Discussion 96
6.5 Conclusion & Future Work 99
7 Conclusion and Future Work 101

BIBLIOGRAPHY 106

LIST OF FIGURES

FIGURE

2.1 A generalized framework for the integration of visual-vestibular signals into a subjective vertical conflict model by using human motion perception. 14

3.1 Visual-vestibular coordinate frame 19
3.2 Visual-vestibular motion sickness (VVMS) model architecture 20
3.3 Visual-vestibular human angular motion perception model. Detailed view of the $SCC_{v\text{-}v}$ block in Fig. 3.A. 22
3.4 Visual-vestibular human linear motion perception model. Detailed view of the $OTO_{v\text{-}v}$ block in Fig. 3.A. 22
3.5 Normalized MS with respect to frequency of lateral oscillation for different model results and experimental data presented by Griffin et al [1]. The orange line represents the no conflict condition and the blue line represents the conflict condition. 26
3.6 Experimentally measured and model predicted responses for passenger motion sickness during experimental runs performed at Mcity under low and moderate vehicle acceleration profiles from Jones et al [2]. Each subfigure shows a different subject. 30
3.7 Experimentally measured and model predicted responses for passenger motion sickness during experimental runs performed during on-road conditions from Jones et al [2]. Each subfigure shows a different subject. 31

4.1 Vehicle platform built for subject trials 36
4.2 Mcity test track and designed path to conduct on-road data collection 37
4.3 UMTRI Motion Sickness Scale with smiley face visual aids that can be shown to study participants 38
4.4 Placement of sEMG sensors on the sternocleidomastoid muscle 40
4.5 Head IMU sensor placement 40
4.6 Sensor suite used during experimental protocol 41
4.7 Timeline for data collection process within the context of the experimental trial 41

5.1 MS Prediction Model Architecture 44
5.2 Correlation analysis for time-based head IMU features 49
5.3 Correlation analysis for frequency-based head IMU features 50
5.4 Regression prediction modeling and validation strategy 57
5.5 Classification expanding window feature engineering strategy 58
5.6 Classification time-offset feature engineering strategy 59
5.7 Custom K-fold validation used for classification 61

5.8 Predicted and true MS scores for (A) NARX (B) LSTM for a representative subject 63
5.9 SVM confusion matrices using time-offset method (n=4) for (A) Binary and (B) Ternary Classification 63

6.1 Physiological Modeling Data Preprocessing Flowchart 69
6.2 Sample Random Forrest confusion matrix for binary classification 89
6.3 Sample Random Forrest confusion matrix for ternary classification 89
6.4 Classification accuracy model performance for different time offsets. 91

LIST OF TABLES

TABLE

2.1 Summary of Motion Sickness Physiological Models in the Literature 12
2.2 Comparison of MS data-driven prediction models across the literature 16

3.1 VVMS nominal model parameters 24
3.2 Sum of residuals between MS model predictions and experimental data corresponding to Fig. 3.6 (scale of 10^4) 29
3.3 Sum of residuals between MS model predictions and experimental data corresponding to Fig. 3.7 (scale of 10^4) 32

4.1 Test conditions and independent variables 38
4.2 Common symptoms and sensations associated with Motion Sickness 39

5.2 Definition of IMU head data dynamic features 45
5.1 Static features considered for model prediction 48
5.3 Relative importance of head motion data streams calculated using the Gini index 51
5.4 Relative importance of head motion features calculated using the Gini index . . 52
5.5 NARX solvers and training functions 53
5.6 LSTM solvers and layers 54
5.7 LSTM model parameters 55
5.8 NARX model parameters 56
5.9 SVM, XG Boost, and Random Forest model hyperparameters 57
5.10 Statistical analysis of LSTM Regression Model performance 62
5.11 Statistical analysis of NARX Regression Model performance 62
5.12 Performance of binary classification models. The bold red text indicates the best performance instance for a given model. 64
5.13 Model prediction results for binary and ternary classification approaches. The results presented correspond to the best-performing feature extraction methods for each model. All models yielded the best results using the time-offset method, with the number of steps ranging between 4 and 6. 64

6.1 Static features considered for model prediction 71
6.2 Definition of Phyisiological data dynamic features 72
6.3 Binary and ternary classification model performance 88
6.4 Classification Model performance for different data normalization techniques. . 90
6.5 Classification Model performance for different BVP data augmentation techniques. 90
6.6 Gini importance for different physiological time-offset windows. 92

6.7 Gini importance for different physiological data streams. 93
6.8 Gini importance for different physiological features. 93
6.9 Effect of removal of static features in model prediction accuracy. 96

ABSTRACT

The impending adoption of autonomous vehicles (AVs) has posed a series of challenges to the automotive industry, with motion sickness (MS) mitigation gaining particular attention. AVs are likely to increase MS incidence due to the occupant's inability to anticipate upcoming vehicle maneuvers and their desire to engage in non-driving related tasks. To design technologies that mitigate MS, it is critical to be able to predict the timing and intensity of occupants' MS response. In the past, theories and models have been created in an attempt to explain and replicate the mechanisms that lead to MS. However, there are no conclusive results that validate their fidelity in terms of MS estimation capabilities. As the first contribution of this thesis, a physiological MS model is proposed, which expands on prior physiological MS models by considering visual and vestibular inputs in three dimensions. The resulting new model is able to capture the effects of visual inputs and provides improved MS estimation compared to prior models, specially in the low frequency range ($< 0.1Hz$). However, it lacks the ability to tailor its prediction towards individual subjects, which can be overcome with the use of data-driven models.

Beyond physiological models, data-driven approaches have been adopted by a limited number of studies to predict MS. However, these models' performance are often limited by the scarcity of MS datasets used for training and the lack of comprehensive time series feature engineering methods. As the second major contribution of this thesis, a machine learning (ML) framework is proposed for the prediction of MS using a comprehensive dataset collected in a previous study. The data used includes self-reported MS scores, sEMG, IMU, and physiological sensor recordings. Both classification and regression predictions have been adopted using various existing ML models. By incorporating lagging features, the proposed ML framework is the first of its kind able to directly capture the effects of past sensor measurements in MS predictions. Another novel attribute of this approach is the ability to consider a priori knowledge of the demographics of the occupants to tailor the prediction of MS, such as susceptibility, sex, and age. The model MS prediction results were assessed in terms of classification accuracy for binary (sick or not sick) and ternary classes (low, medium or high sickness level). The regression model developed was assessed in terms of RMSE values between true and predicted MS scores. The model leveraging head motion data was able

to achieve up to 83% accuracy for binary classification and 61% for ternary classification. RMSE values of 2.1 (on a scale of 0-10) show the ability of the head motion based model to predict the intensity of MS within the same range as the original instruction provided to subjects about the intensity distribution of MS scores. The model leveraging physiological data was able to achieve up to 81% accuracy for binary classification and 58% for ternary classification. A temporal dependency analysis revealed that self-reported MS scores can lag head motion exposure and physiological response by 360s and 180s, respectively. An analysis of the model performance underscored the importance of considering passenger demographics as inputs with the subject's MS susceptibility and subject identifier each contributing to an increase of 7% in model performance. The accuracy results obtained indicate the feasibility of applying these models to on-road applications for MS mitigation.

CHAPTER 1

Introduction and Background

Motion sickness (MS) has been extensively studied to assess passenger comfort in ground, aerial, and maritime vehicles. Further, studies have found that MS is a condition that affects one in every three adults in the United States [3], making it a widespread problem that impacts the daily lives of people who use transportation systems. While limited in-vehicle data has been collected on this matter, the available studies have suggested that passengers are more susceptible to motion sickness than drivers [4, 5, 6, 7]. With the widespread adoption of ride-sharing services and the development of autonomous vehicles (AV), MS has become a pressing issue, given that occupants are increasingly becoming passengers.

Relieved from the task of driving, AV and ride-sharing passengers are also able to engage in non-driving related activities during their rides. However, it has been shown that passenger activities, such as reading or typing on a hand held device, further increase motion sickness [8]. Furthermore, electric vehicles (EVs) have been shown to cause higher motion sickness due to regenerative braking dynamics and the lack of auditory cues regarding vehicle acceleration, such as engine revving [9]. The recent shift in automotive technology and services has led to a greater emphasis on understanding the mechanisms that lead to motion sickness and identifying strategies to improve passenger comfort and productivity.

A fundamental component in addressing these challenges is characterizing passengers' MS response to motion exposure. The characterization of MS in the literature has been primarily done through experimental studies using motion platforms/simulators and test vehicles to a

lesser extent [10, 11, 12, 13]. Motion simulator studies, however, are often not representative of realistic driving conditions that lead to MS since they do not fully replicate car maneuvers that a passenger would experience [14]. For instance, it is difficult for motion simulators to replicate the lateral or centripetal acceleration experienced during a car turn as that would require a large footprint to allow the motion platform seat to reach the required lateral acceleration magnitude. In comparison, MS experimental studies conducted in passenger vehicles driven in realistic driving conditions have several operational challenges including safety considerations, test track access, environmental and route factors, and cost. However, in-vehicle studies are more representative of passengers' experience in naturalistic conditions [15, 2].

In order to be able to better understand MS and to develop technologies to mitigate it, it's critical to be able to predict when someone is going to become motion sick. However, MS response varies as a function of individual subject responses, vehicle motion, and cabin environment conditions [16]. Since MS cannot be measured directly from the occupant, this objective requires a system that is capable of estimating MS based on other variables. As part of a holistic and systematic approach to parameterizing MS, researchers have developed models to simulate the human response to certain motion and visual inputs [17][18][19]. MS prediction models have the potential to be integrated with passenger and vehicle dynamics models to determine how a given route, driving style, and vehicle model can lead to passenger discomfort. MS prediction models also have the potential to identify and evaluate strategies to mitigate MS effectively [20][21]. These models can be broken down into two main categories: physiological models and data-driven models.

The physiological models are based on theories that attempt to explain the physiological mechanisms that lead to MS [17, 22, 23, 24, 25, 26, 27]. One of the key deficiencies of MS physiological models is their inability to accurately predict MS at frequencies below 0.1Hz. Models tend to underestimate the level of MS experiences at this frequency range [19]. One possible explanation for this behavior is that few models consider the contributions of the

visual system to MS, focusing primarily on the vestibular system [26, 27]. It has been shown that the visual contributions to MS play a significant role at low frequencies (¡0.2Hz) [28, 29, 30]. While a few visual-vestibular MS models have been proposed in the literature [31, 32], there is no established framework for handling both linear acceleration and angular velocity using visual-vestibular inputs in three dimensions. These types of inputs are widely present in MS triggering events, such as in the case of a passenger looking at a screen inside a moving vehicle, which can lead to increased MS due to visual-vestibular conflict. It has been shown that increased obstruction of a passenger's view of the outside world leads to increased motion sickness [33]. This can pose a limitation on the ability of existing models to accurately predict MS for realistic in-vehicle scenarios. Hence, taking into account the contributions of the visual field of view of a passenger has the potential to improve MS modeling prediction.

To address the shortcomings of existing MS physiological models, an alternative MS model is proposed in Chapter 3, capable of handling three-dimensional linear and angular visual-vestibular motion stimuli. This accounts for motion that is representative of what occurs in a moving vehicle and further improves MS prediction over the whole frequency range [27, 34]. The proposed improved model is able to achieve this through a novel framework that draws from both a subjective vertical conflict (SVC) motion sickness model and a visual-vestibular human motion perception model. While the human motion perception model provides a way to estimate the visual and vestibular stimuli as a unisensory perceived signal, the SVC model provides a way to quantify the accumulation of this perceived signal as a MS score. In Chapter 3, this model is described, and the model results are compared with experimental MS responses to realistic driving and task performance conditions gathered by Jones et al [8].

While the proposed physiological model improves on the predictive performance when considering visual stimuli, it still has shortcomings associated with the fundamental limitation of the understanding of the mechanisms that lead to MS. Given that physiological

models attempt to create mathematical representations of the body's sensory and information processing mechanisms, the predictive performance of these models is constrained by the limited existing knowledge of the signal processing pipeline of the human central nervous system. On the other hand, data-driven models use motion and physiological data associated with MS to make predictions without establishing a physiological mathematical framework. This enables the determination of input-output relationships between sensory inputs and MS response, leveraging prior observations and machine learning models [35, 36, 37].

A key challenge associated with data-driven models for MS prediction is the scarcity of MS datasets available. Given the aforementioned challenges related to performing MS experiments, limited data is available to train machine learning models to achieve effective prediction capabilities. Jalgaonkar et al [15][38] conducted a study to collect on-road MS response data along with multiple sensory data streams, such as subjects' head motion, blood volume pulse (BVP), electrodermal activity (EDA), and surface electromyography (sEMG). As a result, the study built one of the most extensive MS datasets collected, to the authors' best knowledge, and presented a potential to enable key developments for data-driven models for MS prediction. This experimental protocol is outside of the scope of the contributions of this thesis, but it is described in Chapter 4 to provide context to the dataset used for training the models presented in subsequent Chapters.

Another key challenge associated with data-driven models for MS prediction is establishing a feature engineering framework and a model pipeline to enable accurate prediction capabilities. Since MS is a time-cumulative phenomenon, the feature engineering process requires time-series methods suitable for MS modeling. Chapter 5 presents a new approach to data-driven prediction using a novel feature engineering time-series method capable of combining lagging features with conventional classification models without data loss. Further, the Chapter presents a data processing and model implementation pipeline to standardize machine learning MS prediction models for classification and regression. The Chapter presents these contributions within the use case of passengers' head motion data. It identi-

fies the most relevant features and describes the process of tuning the model parameters to achieve effective prediction.

While IMU data, as used in Chapter 5, has a well-established correlation with respect to MS [39], other data streams, such as physiological data, lack as clear a correlation. Physiological responses to MS symptoms, such as nausea and dizziness, are often mediated by the activation of the sympathetic nervous system, leading to variations in heart rate (HR), electrodermal activity (EDA), respiratory rate (RR), eye movement and others [40]. Given the outlined shortcomings associated with MS data-driven models in the literature and a lack of understanding behind the physiological mechanisms of MS symptoms, identifying relevant data streams and features for MS prediction remains challenging. While models have been presented to attempt to draw correlations between physiological data and MS [41, 42, 43], they often fall short due to the nature of the data collected, the quality of the sensor data, the small sample size, and the lack of a time-series-based framework. Chapter 6 builds on the feature engineering methods and model pipeline presented in Chapter 5 to create an MS prediction model using physiological datastreams, including BVP, EDA, and sEMG. Further, this chapter identifies the most relevant physiological datastreams for MS prediction and their corresponding most relevant features, providing insights that enable a better understanding of the relationship between MS and physiological responses.

In summary, the contributions of this thesis are as follows:

1. In Chapter 3, proposal and assessment of a combined MS physiological model and human motion perception model that;

    (a) Accounts for visual-vestibular linear acceleration/specific force and angular velocity motion stimuli in three dimensions;

    (b) Outputs a quantitative MS rating that is congruent with results from previous studies conducted on motion platforms/simulator over the whole frequency range for angular velocity and linear specific force sinusoidal inputs;

(c) Predicts MS for realistic driving and task conditions and accounts for a wide range of MS symptoms in congruence with experimental results.

2. In Chapter 5, proposal and assessment of a data-driven MS prediction model that;

   (a) Accounts for three-dimensional linear and angular head motion data as an input.

   (b) Leverages subject demographics to make individualized predictions.

   (c) Is trained on a relatively extensive on-road dataset with recurring MS score measurements and different MS mitigation conditions.

   (d) Utilizes novel time-series feature engineering methods to leverage data at past time-steps for classification with 83% accuracy for binary classification and 61% accuracy for ternary classification.

   (e) Deploys a framework to perform deep learning regression of MS scores and achieves a Root Mean Squared Error (RMSE) of 2.1 on a 0-10 scale.

   (f) Establishes a mathematical foundation for understanding the temporal dependency of MS response on head motion data, identifying that self-reported MS scores can lag head motion exposure by 360 seconds.

3. In Chapter 6, proposal and assessment of a data-driven MS prediction model that;

   (a) Achieves the same as items 2 (b)-(c) and,

   (b) Leverages physiological (EDA, BVP and sEMG) data as an input.

   (c) Utilizes novel time-series feature engineering methods to leverage data at past time-steps for classification with 81% accuracy for binary classification and 58% accuracy for ternary classification.

   (d) Provides a comparison analysis of the most important physiological features for MS prediction, highlighting the importance of EDA and sEMG for MS prediction.

(e) Establishes a mathematical foundation for understanding the temporal dependency of MS response on physiological data, identifying that self-reported MS scores can lag head motion exposure by 180 seconds.

CHAPTER 2

Literature Review and Gaps in Current Research

2.1 Physiological Models for Motion Sickness

According to the sensory conflict theory, motion sickness arises when the brain receives conflicting inputs from the visual, vestibular, and proprioceptive systems [44, 45, 46, 47]. In particular, the two most prevalent types of sensory conflicts are the canal-otolith conflict [44] and visual-vestibular conflict [25]. Given observations that subjects without a functioning vestibular system do not suffer from MS, the canal-otolith conflict is considered to be a causative factor of MS, while the other integrated sensory conflicts (such as visual-vestibular) are considered to be secondary factors of MS. The sensory conflict theory has been shown to have large congruence with experimental results. Further, the canal-otolith conflict specifically has been used to create MS models in the literature due to its practical implementation in a mathematical framework. However, models have faced limitations in integrating visual and proprioceptive systems within the framework of the mechanism of this theory to achieve accurate predictions [31, 32].

A subset of the sensory conflict theory, the subjective vertical conflict (SVC) theory states that motion sickness arises due to a difference between the subjective vertical predicted based on previous experience and the vertical as perceived by the sensory systems [48, 17, 23, 49]. The subjective vertical is the result of an internal model, which behaves as a learning

mechanism within the central nervous system. The internal model attempts to duplicate the dynamics of the sensory system to minimize the discrepancy between the subjective vertical and the sensed vertical. The estimation of the subjective vertical is a result of a neural filtering process that attempts to differentiate inertial and gravitational accelerations, which creates inherit lag in the system [17]. This causes the subjective vertical to deviate from the sensed vertical, especially for relatively large magnitude stimuli at the relevant frequency range (0-1Hz), ultimately resulting in motion sickness. The SVC theory can be used for MS model development as the sensed and subjective verticals can be quantified in terms of its direction and magnitude, allowing for a correlation between the conflict and a quantitative motion sickness score prediction [17, 22]. While this theory can be expanded to include any sensory system that is able to perceive motion, the vestibular and visual systems are often considered the most relevant [44].

While other MS theories are prominent in the field, such as the postural instability theory [50], the theories described above are the most relevant for the purposes of the model presented in this paper, as they enabled the prior development of a mathematical framework for the mechanisms of MS. MS theories have led to the development of various models that attempt to predict motion sickness given certain visual, vestibular, and proprioceptive inputs. To provide a quantitative output of MS, these models rely on numeric scales that have been previously developed in experimental studies.

Some scales provide measures of MS based on the presence of fixed, explicit symptoms, such as the Motion Sickness Assessment Questionnaire (MSAQ) scale. Other scales use self-reported symptoms as part of quantifying MS, such as the Fast Motion Sickness (FMS) scale. Hence, each of these scales cannot fully capture the motion sickness experienced by subjects since MS affects subjects through different symptoms of varying magnitudes. Consequently, the performance of MS models will have different limitations depending on the scale being used.

For example, the commonly used Motion Sickness Incidence Index (MSI) scale has been

defined as the percentage of subjects that vomit under a sinusoidal motion with certain magnitude and frequency [51]. The applicability of this scale to studying MS in AVs is potentially limited as passengers are expected to show a wide range of symptoms prior to vomiting. Another frequently used scale for MS is the MSQ scale, which is based on a questionnaire that assesses symptoms such as headache, fatigue, nausea, stomach awareness, blurred vision, cold sweating and vertigo [52]. Another commonly used scale is the MSSQ scale, which uses a questionnaire that can account not only for symptoms, but also for the subject's susceptibility to MS [53]. Both the MSQ and MSSQ scales are limited by the symptoms they encompass as well as the subjectivity of self-reported symptoms. Other scales such as FMS and MISC [54] are prone to similar limitations. Jones et al. [2] suggested a new rating scale that captures the spectrum of MS symptoms and physiological indicators during realistic driving conditions, making it pertinent to studies that involve MS prediction applied to AVs. In this scale, participants were asked to rate their MS from '0' (no MS at all) to '10' (need to stop the vehicle). They were also instructed to describe in their own words and rate any MS sensations they experience throughout the testing protocol. The descriptions provided were processed and standardized to the MS score. This allows for subjects to express their MS beyond a predetermined list of symptoms while taking into account their own subjective rating and perception of symptoms. This allows for the assessment of a wide array of symptoms and intensities, which can be advantageous under realistic driving conditions, where multiple symptoms might be present. The model proposed in this paper is compared to the results in the scale proposed by Jones et al.

Key physiological motion sickness models presented in the literature are summarized in Table 1; the table includes the model inputs and outputs, their limitations, the nature of visual information and the number of degrees of freedom (DoF). The DoFs are defined in this table as the number of independent visual-vestibular signals along a given direction (i.e. vertical visual angular velocity and vertical vestibular angular velocity are counted as 1 DoF). It is important to note that most models' performance have been compared with

experimental results often obtained from studies conducted on motion platforms/simulators that do not represent realistic vehicle motion.

The SVC theory has been extensively used in the literature to develop models to predict MS due to the efficiency of computing the conflict between the sensed and subjective verticals. The initial model proposed by Bos et al. [17] and later adapted by Kamiji et al. [22] showed congruence between simulation results and the experiments performed by McCauley et al [55]. However, when Kamiji attempted to apply the model to replicate Griffins et al. [1] data, it was observed that the simulation results underestimate motion sickness when the input lateral acceleration frequency was below 0.1Hz. This can be explained by the fact that Griffin's dataset was collected under the presence of a visual-vestibular conflict, as the subjects were enclosed in a moving cabin and exposed to sinusoidal motion with no view of the external environment. Hence, a possible explanation for the deviation between Kamiji's model results and Griffin's data is that Kamiji's model doesn't account for the visual contribution to MS. The basis for this claim is that the visual component contributes to motion sickness, especially at the low frequencies (<0.2Hz) [29], at which Kamiji's model was inaccurate. Braccesi et al. [31] attempted to adapt Bos' SVC model by considering both visual and vestibular components to predict MS. However, Braccesi's model only provides a framework to handle linear acceleration visual-vestibular inputs, and not angular velocity. Since angular motion is expected in a moving vehicle, it is important for models to capture both linear and angular motion in all three dimensions. Wada et al. made further adaptations to Kamiji's model to optimize the model parameters [58] and to account for the visual contribution of angular velocity [32]. However, Wada's model still lacks the ability to handle linear visual inputs, making it not applicable in situations where there is presence of a linear visual-vestibular conflict. Hence, there is still a lack for a physiological model that captures visual-vestibular linear and angular motion stimuli in three dimensions to predict MS over the entire relevant frequency range (0.01-0.5Hz).

Based on the identified gaps in the models presented in the literature, physiological MS

Table 2.1: Summary of Motion Sickness Physiological Models in the Literature

#	Authors	Year	Type of Model	Inputs / Outputs	Assumptions / Limitations	Degrees of Freedom	Visual Info
1	McCauley et al. [55]	1974	Vestibular	I: Vertical force, O: MSI	Limited to specific force only, and vestibular influence	1 DoF	None
2	Oman et al. [24, 49]	1982, 1989	Visual-Vestibular	I: Sensed motion by visual and vestibular sensors O: Subjective Discomfort	Heuristic model for sensory dynamics, only outputs subjective discomfort. First model to propose internal observe	Not defined	Not defined
3	Bos et al. [17]	1998	Vestibular	I: Sensed specific force of vertical motion O: MSI	Only vestibular model, no influence of visual sensory system considered	1 DoF	None
4	Atsumi et al. [56]	2002	Other	I: Vertical specific force, roll and pitch of vehicle O: Motion sickness level	Output is not in a standard motion sickness scale, correlation model with no physiological modeling	3 DoF	None
5	Kamiji et al. [22]	2007	Vestibular	I: Sensed motion by vestibular sensors (specific force and angular velocity) O: MSI	Only vestibular model, no influence of visual sensory system considered	6 DoF	None
6	Khalid et al. [23]	2011	Vestibular	I: Sensed motion by vestibular sensors (specific force and angular velocity) O: Weighted MSI, combination of horizontal and vertical MSI	Only vestibular model, no influence of visual sensory system considered, designed for contemporary ships	6 DoF	None
7	Braccesi et al. [31]	2011	Visual-Vestibular	I: Sensed motion by vestibular sensors (specific force), visually perceived linear acceleration O: MSI	Only acceleration, no influence of angular velocity modelled. Uses all acceleration conflicts to predict motion sickness	3 DoF	Linear accel only
8	Salter et al. [26]	2020	Other	I: Field of view, motion of passenger head O: MISC	Data correlation that uses vehicle motion, passenger gaze, and passenger motion. Motion passenger head predicted using multibody dynamics.	3 DoFs are used for specific force. Visual DoF is undefined per this paper's definition	Undefined weighting
9	Wada et al. [32]	2020	Visual-Vestibular	I: Sensed motion by vestibular sensors (specific force and angular velocity), visually perceived angular velocity O: MSI	Uses camera images to predict visually perceived motion, builds on Bos et al.	6 DoF	Angular velocity
10	Wada et al. [57]	2021	Vestibular	I: Sensed motion by vestibular sensors (specific force) O: MSI	Only vestibular model, no influence of visual sensory system considered	3 DoF	None

models would benefit from an integration of the visual-vestibular interaction framework to allow for an improvement in MS prediction. To do so, it is necessary to establish an architecture that allows for the integration between the visual and vestibular stimuli. Bos et al. proposed a theoretical framework for the integration of visual-vestibular interaction and subjective vertical conflict models [59]. In Bos' framework, the interaction between the visual and vestibular systems results in the sensed body states, which can be compared to the output of the internal model in order to calculate motion sickness.

Figure 3.1 shows a proposed simplified framework that allows for the integration of the visual-vestibular signals within the context of subjective vertical conflict models. Braccesi showed that human perception models are suitable for modeling the visual-vestibular interactions by assuming that the sensed body states are effectively perceived motion (ref). The perceived motion as a result of human perception modeling can be compared to the expected motion resulting from the internal model in order to yield a quantifiable measure of motion sickness. However, Braccesi's model only account for linear motion, limiting its applicability to situations in which angular velocity plays a significant role, such as when traveling in a vehicle.

Zacharias [34] proposed a human motion perception model for angular velocity and Telban et al. [27] expanded on this work by proposing a human motion perception model for linear velocity. For the purposes of the model presented in this paper, the human motion perception model proposed by Telban et al. is used.

Based on the gaps identified in the literature and on the framework for the integration between human motion perception and the SVC theory, in Chapter 3, an improved model is proposed that

1. Combines a 3D SVC model with a human motion perception model;

2. Accounts for visual-vestibular linear acceleration/specific force and angular velocity motion stimuli in three dimensions;

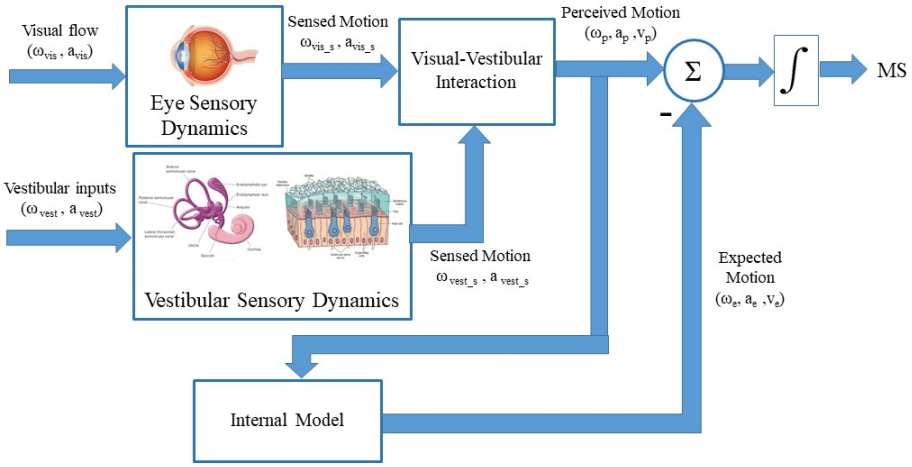


Figure 2.1: A generalized framework for the integration of visual-vestibular signals into a subjective vertical conflict model by using human motion perception.

3. Outputs a quantitative MS rating that is congruent with results from previous studies conducted on motion platforms/simulator over the whole frequency range for angular velocity and linear specific force sinusoidal inputs;

4. Predicts MS for realistic driving and task conditions and accounts for a wide range of MS symptoms in congruence with experimental results.

2.2 Data-Driven Models for Motion Sickness

Table 2.2 lists the 15 previously developed data-driven MS prediction models in the literature, to the best of this author's knowledge. The columns of Table 2.2 represent relevant data acquisition methods, model configurations, and performance metrics for each model. As seen in Table 2.2, only 2 data-driven MS prediction models in the literature have used head motion data as an input to make its prediction, and they did so for virtual reality (VR) applications and not on-road applications. Hong et al. used mathematical objective functions to make

MS predictions based on the head motion data [60]. However, the actual MS prediction module is the subjective vertical conflict (SVC) model proposed by Kamiji et al. [19]; hence, it is not included in this literature comparison. Further, none of the models assessed use participant demographic data (e.g. gender and age) as an input to make model predictions. Given the high variability in MS susceptibility across different demographics, this type of data input can significantly improve model generalizability.

The average total duration in minutes for the datasets considered in the previous models is 698 minutes, with only three datasets surpassing the 1000-minute mark. Among the datasets with over 1000 minutes, only one collected MS data at regular intervals during their trials. This showcases the scarcity of in-vehicle on-road data to train and validate the existing models. Of the 15 models considered, only 4 collected their data using a test vehicle [61][62][43][41]. Additionally, none of the models considered were trained on a dataset including a test condition attempting to mitigate the subjects' MS. Since one of the key benefits of using an MS prediction model is to inform MS mitigation strategies, the lack of a test condition of this nature limits the extent to which the existing models can be used for such application. Lastly, these models have yet to use techniques to leverage data from previous time steps to make time-series predictions of MS. This is even when prior literature on MS theories has suggested that MS is a time-cumulative phenomenon, which indicates that capturing data trends from previous time steps should be a pertinent attribute for model development [17]. The primary use case for these models is on the design and modulation of MS mitigation technologies, which requires the ability to perform predictions in real time. In that sense, using past time windows for real-time prediction is critical for model performance when taking into account that the model does not have access to data corresponding to an entire ride (i.e. future time windows.)

Another key requirement for developing MS models is the ability to identify the most relevant data streams and features to use as inputs to the model [73]. Using features with low relevance for prediction can lead to high-dimensionality datasets, which can have a

Table 2.2: Comparison of MS data-driven prediction models across the literature

Authors	**Model**	**Motion/Test**	**Total dataset length (min) / Recording frequency (min)**	**Input**
Bang J. S et al, 2023 [61]	CNN	On-road/No mitigation	1748/1	EEG
Ren et al., 2023 [62][36]	SVM	On-road/No mitigation	390/5	Cerebral blood oxygen signals (fNIR 200C imager)
Tan et al, 2022 [43]	SVM, Random Forest, Xgboost, ANN, CNN	On-road/No mitigation	120/1	HR, EDA, fNIRS, STP, PPG.
Henry et al., 2022 [41]	Linear/Polynomial	On-road/No mitigation	1600/0.5	ECG, EDA, HR, RSP, SKC
Ramaseri Chandra et.al [63]	KNN, SVM, RF, GB	VR/No mitigation	60/1	IMU Head
Salehi et al.[64]	GB, RF, SVM, KNN, Logistic regression, Decision tree	VR/No mitigation	15/0.08	IMU Head
Hua et al., 2023 [65]	LSTM, BiLSTM	VR/No mitigation	644/10.73	EEG
Keshavarz et al, 2022 [42]	Random Forest	Stereoscopic Videos/No mitigation	630/1	ECG, EDA, EGG, RSP, SKT, IMU
Recenti et al., 2021 [66]	Random Forest	Gradient Boosting Tree, AdaBoost, SVM, KNN, Multilayer Perceptron	VR, moving platform/No mitigation 130/1x per trial	EEG, EMG, HR
Li et al., 2019 [67]	SVM, One-Against-One	VR/No mitigation	540/Continuous	EEG
Lee et al., 2019 [68]	CNN, NN	VR/No mitigation	109/1x per trial	Video frames
Padmanaban et al, 2018 [69]	Bagged Decision Trees	VR/No mitigation	109/1x per trial	Video frames
Kim et al, 2022 [70]	SVC Conflict, CNN, Activation function for classification	VR/No mitigation	4158/1x per trial	Video frames
Lin et al., 2012 [71]	SVM, One-Against-One	360o video, Motion Simulator 6 DoF/No mitigation	750/Continuous	EEG
Liao et al, 2020 [72]	LSTM, Activation Classification	VR/No mitigation	3900/Random	EEG

detrimental effect on model training and can lead to issues such as overfitting [74]. Given the inaccessibility to specific data streams during real-world applications, understanding the relative importance of these data streams can enable effective predictions when sensor data is

only partially available. In addition, understanding the relative importance of data streams can enable a better understanding of the mechanisms that elicit MS and the physiological responses associated with them. None of the models considered in Table 2.2 provides a framework to compare the relative importance of data streams.

The insights from the literature review presented in Table 2.2 make it evident that there are still significant gaps in the data-driven modeling efforts for MS prediction in terms of modeling approach and dataset comprehensiveness. These gaps include (i) lack of head motion data as an input, (ii) non-consideration of participant demographics, (iii) short total time duration for data collection, (iv) lack of MS data collected at regular intervals during the trials, (iv) lack of exposure to on-road in-vehicle motion, (v) absence of a test condition that captures MS mitigation strategies, (vi) lack of a framework that handles past data for continuous time series prediction and (vii) absence of data stream and feature importance analysis. Chapter 4 describes the experimental protocol used to collect the dataset leveraged by the models proposed in subsequent chapters. Chapter 5 proposes a new approach to data-driven MS prediction using feature engineering and machine learning methods based on passenger head motion data. Chapter 6 builds on this approach and applies it to create a data-driven physiological model and to analyze the relative importance of physiological data streams in MS prediction. This addresses the gaps mentioned earlier (i-vii) and is closer to a realistic and functional implementation of MS prediction for on-road in-vehicle applications.

CHAPTER 3

A Visual-Vestibular Model to Predict Motion Sickness for Linear and Angular Motion

3.1 Proposed Model

Chapter 2 outlined the gaps with physiological and data-driven models for MS prediction. The work presented in this thesis attempts to address the deficiencies with both types of models. In this section, the work on improving the prediction capabilities of physiological models is presented by proposing a visual-vestibular motion sickness (VVMS) model to predict the motion sickness index (MSI) as a function of visual and vestibular inputs. The general framework established in Chapter 2 was used to combine a 3D SVC model with a motion perception model. This model expands on the previously developed VVMS model proposed in Jalgaonkar et al [75] by accounting for the linear component of the visual input. The model combines the three-dimensional vestibular SVC model proposed by Kamiji [19] with the visual-vestibular perception model proposed by Telban et al.

The model's ability to capture visual-vestibular linear and angular motion in three directions makes it applicable to passenger activities, such as interacting with a handheld device or facing forward and looking out the vehicle window. It also makes it applicable to other MS triggering events such as seasickness and cybersickness. However, comparison of the model results with real world data has only been performed with respect to motion simulators and car sickness data.

For the purposes of the model presented, it was assumed that the visual and vestibular coordinate frames are collocated and co-aligned as shown in Fig. 3.1. It was assumed that such reference frame is placed as the midpoint of the line connecting the two ears, intersecting the Frankfurt plane. This assumption allowed for a unified reference frame for the visual and vestibular sensing systems considered. The model framework is shown in Fig. 3.2 and its details are discussed next.

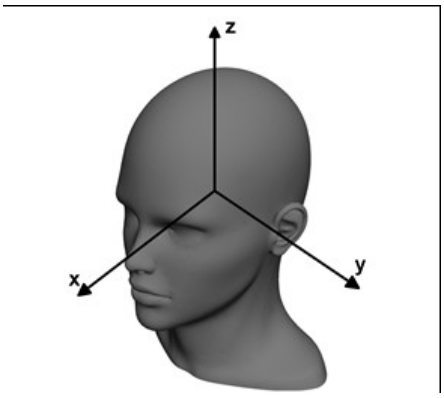


Figure 3.1: Visual-vestibular coordinate frame

The inputs to the model are $\mathbf{a}$, ω, $\mathbf{a_{vis}}$, $\omega_{\mathbf{vis}}$, which are vectors with three degrees of freedom defining the inertial linear acceleration of the head with respect to the world reference frame, the angular velocity of the head with respect to the world reference frame, the visual perception of inertial linear acceleration with respect to the visual background and the visual perception of angular velocity with respect to the visual background, respectively. These inputs are defined in terms of the coordinate frame proposed in Fig 3.1, so any data collected on the world reference frame must be resolved appropriately. This resolution is performed through a coordinate frame transformation based on the resting posture of subjects before the trial has started. It has been proposed in the literature that the visual system can sense linear velocity and not acceleration [34]. To account for this, Telban [27] proposes that the visual inertial velocity can be differentiated to obtain visual inertial acceleration. While this is a mathematical tool, it does not represent the true cognitive processes associated with the visual signals. In addition to visual velocity, Bos et al. [59] proposed that the visual

system is able to detect the orientation of gravity. In this model, it is assumed that the visual system is able to estimate the true direction and magnitude of gravity. This allows for the quantification of the difference between visual and vestibular signals as part of the motion perception modeling.

Limited work has been done to quantify the visual input in unstructured environments, such as the inside of a vehicle cabin. Wada et al. [32] proposed that the visual angular velocity input can be estimated using the optical flow of a video through the Farneback method. For the purposes of testing the VVMS model, only two conditions of visual angular velocity inputs are considered: (i) the visual inertial input is equal to zero, which is like the case of a passenger reading inside a moving vehicle; and (ii) the visual inertial input is identical to the vestibular input, similar to the case of a front seat passenger inside a moving vehicle with an unobstructed view of the exterior surroundings.

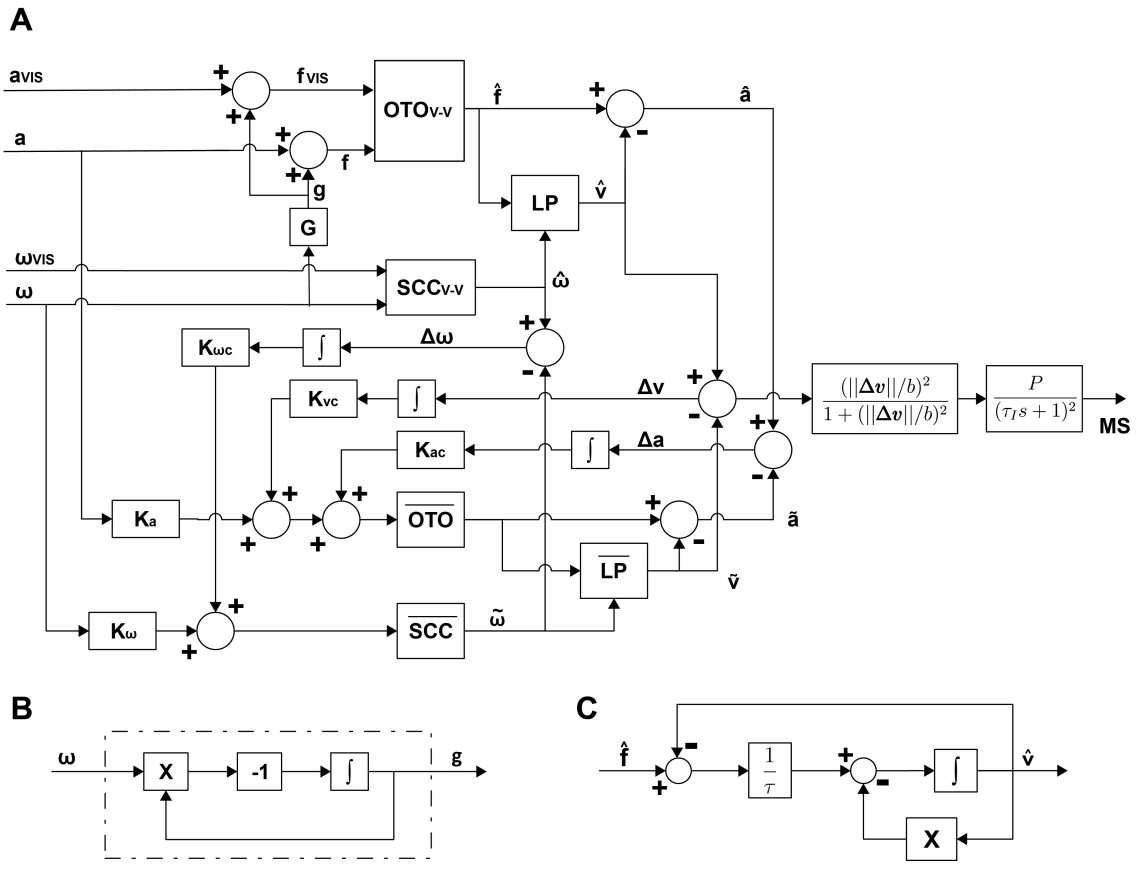


Figure 3.2: Visual-vestibular motion sickness (VVMS) model architecture

This Chapter focuses on the addition of the $OTO_{v\text{-}v}$ and $SCC_{v\text{-}v}$ blocks to the model described in Jalgaonkar et al [75]. These blocks are subsystems of signals and transfer functions that are further elaborated in Figs. 4 and 5.

In order to build the model shown in Fig. 3.2, the generally accepted sensory conflict theory was restated in terms of a conflict between a vertical as perceived by the sensory organs and the subjective vertical as determined on the basis of previous experience. Second, this concept was integrated with estimation theory by the use of an internal model. Physically, the otolith cannot differentiate between gravitational acceleration and inertial acceleration. Thus, the otolith senses the combined gravito-inertial acceleration (GIA), as shown below.

$$f = a + g$$

$$\frac{dg}{dt} = -\omega \times g$$

Where '**a**' is the inertial acceleration and g is the gravitational acceleration. The G block in Fig. 3.2.B accounts for the change in the direction of gravity with respect to the head reference frame and the relationship is captured by taking a derivative of '**g**' with respect to time, as shown in the equation above. The LP block (see Fig 3.2.C) is defined according to an otolith canal model in which the perceived subjective vertical can be estimated through a low pass filter with the following relationship.

$$\frac{d\hat{v}}{dt} = \frac{1}{\tau}(\hat{f} - \hat{v}) - \hat{\omega} \times \hat{v}$$

Here, τ is the low pass filter time constant. The first term on the right hand side gives the estimate of gravity by otolith afferents only, while the second term gives the change of gravity due to rotation only.

The sensory system model is defined by the architecture that encompasses the otolith visual-vestibular interaction model ($OTO_{v\text{-}v}$), the semicircular canal visual-vestibular inter-

action model ($SCC_{v\text{-}v}$) and the otolith-canal interaction model (LP). The outputs of the sensory model are the human perceived dynamics with respect to the world reference frame, consisting of the perceived gravito-inertial acceleration (GIA), perceived angular velocity and perceived vertical, which are defined as $\hat{f}, \hat{\omega}, \hat{v}$ respectively.

The $SCC_{v\text{-}v}$ model follows the angular human motion perception architecture proposed by Telban [27], shown in Fig. 3.3, to estimate the perceived angular velocity because of both visual and vestibular input signals. Similarly, the $OTO_{v\text{-}v}$ model follows the linear human motion perception architecture proposed by Telban, shown in Fig. 3.4, to estimate the perceived GIA because of both visual and vestibular linear input signals.

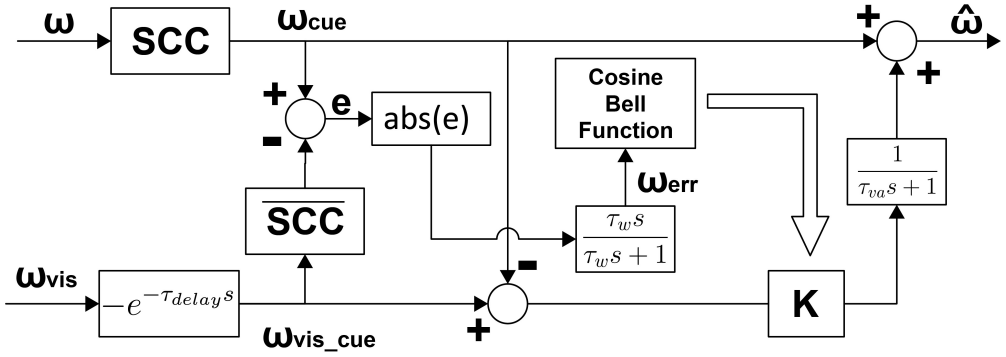


Figure 3.3: Visual-vestibular human angular motion perception model. Detailed view of the $SCC_{v\text{-}v}$ block in Fig. 3.A.

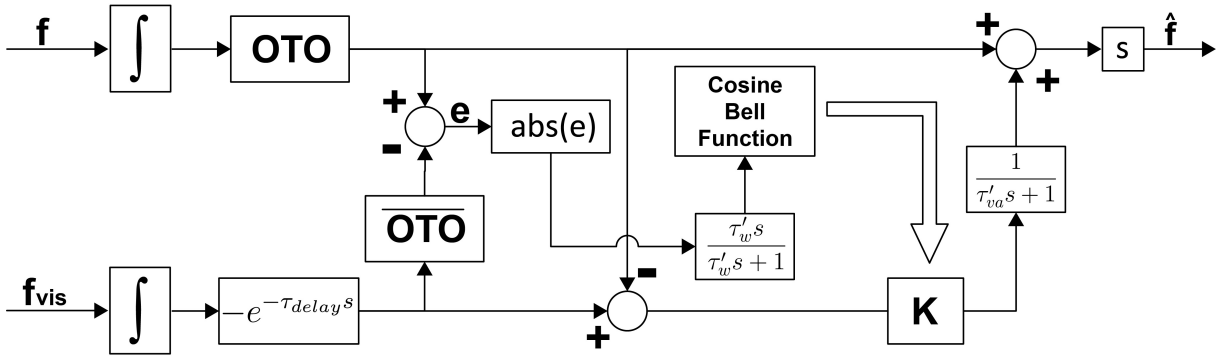


Figure 3.4: Visual-vestibular human linear motion perception model. Detailed view of the $OTO_{v\text{-}v}$ block in Fig. 3.A.

The $SCC_{v\text{-}v}$ block shown in Fig. 3.3 accounts for the coupling of visual and vestibular

angular velocity. The input visual signals for both linear acceleration and angular velocity have an associated time delay defined by τ_{delay}, which accounts for the delays of the visual receptors, the neural transmissions and the processing during motion perception. The angular velocity visual signal is passed through a sensory internal model of the semicircular canals $\overline{\text{SCC}_{\text{vis}}}$ to produce a predicted vestibular signal that can be compared to the actual vestibular signal. It is assumed that the $\overline{\text{SCC}_{\text{vis}}}$ transfer function is a perfect copy of the SCC transfer function, which was defined experimentally by Haslwanter [76], such that:

$$\omega_{cue_i} = \frac{\tau_d \tau_a s^2}{(\tau_d s + 1)(\tau_a s + 1)} \omega_i \quad (i = x, y, z)$$

Where τ_a and τ_d are second order high pass filter time constants. The absolute value of the difference between the vestibular and visual cues passes through an adaptation operator to allow for long-term resolution of steady-state conflict. This adaptation operator is defined as a first order high pass filter with time constant τ_w, and its output is a conflict signal ω_{err} . The optokinetic gain K is computed as a function of err using a modified cosine bell function with conflict threshold ϵ, shown in Fig. 4. The difference between the visual and vestibular cues is multiplied by the optokinetic gain and an optokinetic influence transfer function, which consists of a low pass filter with time constant τ'_{va}. This optokinetic influence represents the gradual build-up of self-velocity, or vection, and its output is added to the vestibular cue to yield the perceived angular velocity.

The $\text{OTO}_{\text{v-v}}$ block accounts for the coupling of visual linear specific force and vestibular linear specific force. These pass through an integrator in order to yield visual and vestibular linear velocity. The remaining structure of the $\text{OTO}_{\text{v-v}}$ block is like that of the $\text{SCC}_{\text{v-v}}$ block, but with different model parameters τ'_w, τ'_{va} and ε'. Further, it is assumed that the otolith transfer function is a unity gain as proposed by Bos et al [17]. The visual-vestibular perceived velocity can then be differentiated to yield perceived specific force. Thus, the output of the $\text{OTO}_{\text{v-v}}$ block is the perceived GIA. Table 3.1 shows the nominal model parameter values

from Kamiji et al. and Telban et al. [22, 27].

Vestibular System		**Visual System**	
Parameter	**Value**	**Parameter**	**Value**
K_ω	0.8	τ_w	8s
K_a	0.1	ε	1.6 deg/s
$K_{\omega c}$	5	τ_{va}	1.6s
K_{vc}	5	τ_{delay}	90s
K_{ac}	1	τ'_w	1s
P	85	ε'	0.2 m/s
τ_l	720s	τ'_{va}	1.6s
B	0.5 m/s^2	–	–
τ_d	7s	–	–
τ_a	190s	–	–
OTO	1	–	–
τ	5s	–	–

Table 3.1: VVMS nominal model parameters

3.2 Results and Discussion

To assess the performance of the proposed model with respect to MS triggering events in controlled environments, we compared our model results with data collected by Donohew and Griffin et al [1] for lateral oscillations. In this experiment, subjects could not see the external environment, meaning there was a visual-vestibular conflict. To enable the comparison between the model results and Griffin's data, it was necessary to find a common scale for the two, which was achieved by normalizing MS score by the highest observed score.

The VVMS model was assessed based on two conditions, one in which the visual input

was identical to the vestibular input (simulating no sensory conflict) and one in which the visual inertial input was equal to zero (simulating sensory conflict). Note that under the second condition, there is still a visual component of gravity present as explained in the previous section. The two model results were compared to Griffin's data as a function of frequency of lateral oscillation, as shown in Fig. 3.5. Griffin normalized the data such that the highest score observed would correspond to a rating of 1. The model replicated this standardization by normalizing the highest MS score under the same conditions to 1. It is possible to observe that the model response for the conflict condition had larger agreement with respect to the experimental data below 0.2Hz as compared to the no conflict condition. The no conflict condition corresponds to the same model prediction as Kamiji et al [19] model and can be used for benchmark purposes. This improvement is aligned with the expected behavior as visual stimuli causes higher MS in the low frequency region. The model results for the conflict condition were slightly worse in the frequency region above 0.2Hz. When considering the entire frequency region (0.01-0.8Hz), the model performed better under the conflict condition. This is expected as subjects of the Griffin dataset were exposed to MS triggering motion under a visual-vestibular conflict condition. This supports the notion that the integration of linear human motion perception and subjective vertical conflict models leads to an improvement in MS prediction.

By comparing model results to the Griffin dataset as seen in Figure 3.5, it was shown that the VVMS model improves MS prediction for prescribed motion profiles generated by motion platforms/simulators. However, motion simulators are not able to capture the conditions a passenger would experience in a moving vehicle To further compare the model results with realistic driving experimental data, 8 subjects' data were used from the experiments conducted by Jones et al [2].

Jones et al. gathered motion sickness data from passengers during test-track and on-road driving conditions [2]. The test-track scripted route was completed at two different acceleration levels on the Mcity closed test facility. The on-road scripted routes were completed on

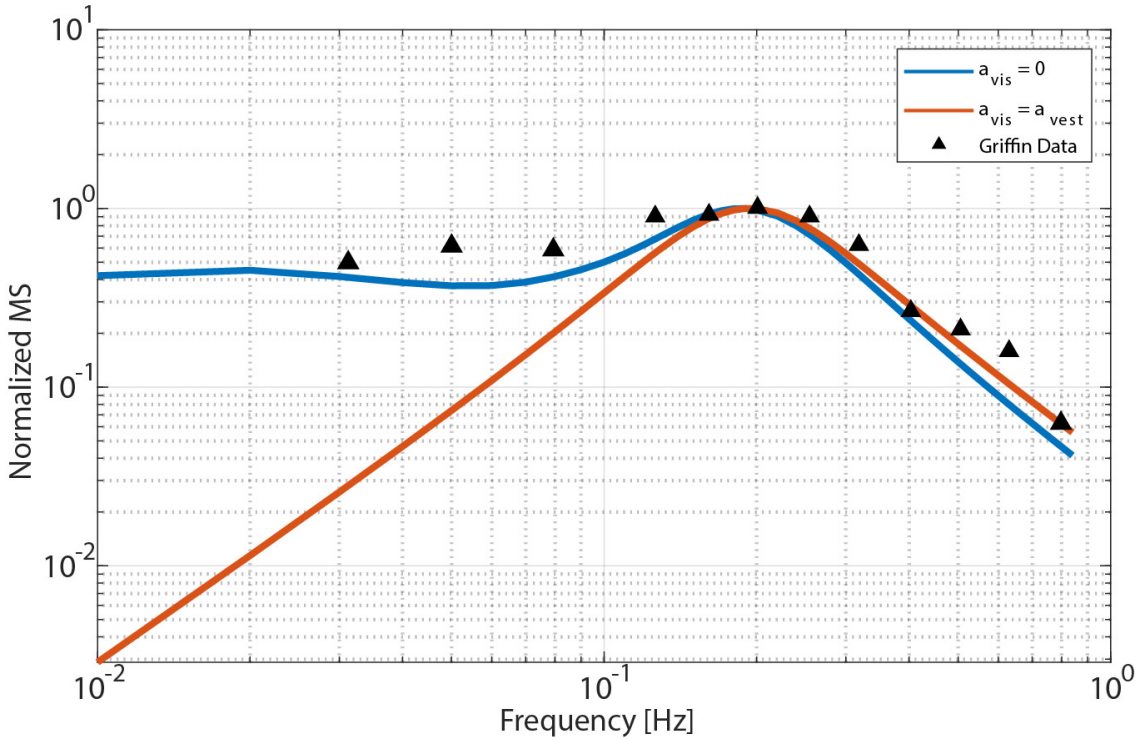


Figure 3.5: Normalized MS with respect to frequency of lateral oscillation for different model results and experimental data presented by Griffin et al [1]. The orange line represents the no conflict condition and the blue line represents the conflict condition.

local Ann Arbor roads (urban route) and Michigan highways (highway route). The on-road routes were approximately 55min in duration, while the Mcity route was approximately 20min in duration. For each, MS ratings were obtained during every 1-minute of the in-vehicle exposure. The dataset included a total of eight subjects with two subjects from each route condition. These conditions consisted of (i) an urban route, (ii) a highway route, (iii) a low acceleration level of a scripted route and (iv) a moderate acceleration level of a scripted route. Conditions (iii) and (iv) were performed at the Mcity test facility, while conditions (i) and (ii) were performed on Michigan roads. Each subject was exposed to the same route twice, once in which they were instructed to face forward with an unconstrained head posture (*no-task*), and once in which they performed a task on a handheld device (*task*). Subjects were asked to self-report the frequency at which they become motion sick between 'never', 'rarely', 'sometimes' and 'frequently'. The following is the occurance of self-reported motion

sickness frequency for each corresponding test condition: (i) one 'rarely', one 'sometimes' (ii) one never, one 'sometimes', (iii) one 'never', one 'frequently' (iv) two 'sometimes'.

The passengers' head motion was recorded using IMUs that provided angular velocity and linear acceleration in 3 directions. The IMU data was used as an input to the model to replicate the sensory information of the otolith and semicircular canals. To account for the orientation of the IMU mounted on the passenger's head, the rotation matrix between the passenger's initial head acceleration and the acceleration of gravity was determined based on accelerometer data. The collected IMU data was then multiplied by the rotation transformation matrix that aligned the passenger's initial head orientation with the world reference frame. Both linear acceleration and angular velocities were acquired at 100Hz and filtered using a Gaussian Filter with a moving window of 80 data samples.

During the (*no-task*) condition, passengers adopted an unconstrained head posture and gaze, for which the visual inputs were assumed to be identical to the vestibular inputs. This assumption is based on a naturalistic passenger behavior study conducted by Reed et al. that showed front row passengers directed their gaze outside the windows of a vehicle close to 68% of the time (Reed, 2020). For the (*task*) condition, passengers performed visual-based tasks on a handheld device, for which the visual inertial input was assumed to be zero. It is assumed that the passenger views the device as an approximate static object, despite movements on the peripherals of the field of view. Notice that the act of performing a task in itself may be a confounding factor [77, 78]. Future work may include improve estimates of the visual input using head-mounted cameras or other visual tracking methods.

Given that the SVC model was originally built to reflect results congruent with experimental data acquired using the MSI scale, it was necessary to change certain model parameters to account for the Jones et al. [2] scale. While there is no direct correspondence that can be traced between the two scales, parameter tuning can provide results that approximate the observed response. The parameter 'P' was modified to a value of 10 to reflect the maximum possible MS rating of the Jones scale. In addition, the parameter τ_I was significant in the

replication of such results as it dictates the rate at which MS accumulates over time. In order to determine the optimal τ_I that fits the experimental data, the following optimization problem was solved

$$\sum_{j=1}^{M}\sum_{i=1}^{N} ||MS_{model_{i,j}} - MS_{experimental_{i,j}}||$$

Where j corresponds to the subject index, M is the number of subjects assessed, i corresponds to the instance of input IMU data, N is the number of IMU data points in the experimental runs, MS_{model} is the model output, and $MS_{experimental}$ is the moving average of the subject's MS response with a window of 5 minutes. The result of this procedure yielded a value of τ_I equal to 216s.

Preliminary observations suggested that the model was underestimating motion sickness for the conditions in which the passenger performed a task. One hypothesis for this is that the model doesn't account for the cognitive resources associated with completing the task. It has been shown that performing a task in a moving vehicle increases MS response, often causing the passenger to cease the task at hand [2]. We hypothesize that passenger task performance contributes to MS not only through the introduction of a visual-vestibular conflict, but also through the addition of cognitive processing requirements. Previous studies have found a relationship between cognitive load and cybersickness [77, 2, 78], but there is a lack of passenger vehicles studies on this matter. The proposed hypothesis is also aligned with the multiple resource theory, which states that mental operation performance degrades when the available attention resources are insufficient [79, 80]. Inconsistencies across studies warrants further studies to understand the impact of task workload on MS. An alternative hypothesis for the model's underestimation of MS is that the assumption of zero visual inertial input during task performance doesn't effectively capture the passenger's gaze movement. To address this discrepancy, we decreased the value of the learning feedback gains of the internal model. Modifying the value of K_{ac}, K_{vc}, K_{wc} to 50% of the original values yielded results with higher congruence when compared to the experimental data for *task* conditions.

With these model adaptations, the predicted MS response was compared to the observed

MS response to assess the model's performance. The subject's self-reported MS data in the previously discussed Jones et al scale [81], along with the model predicted outputs for the Mcity subjects are shown in Fig. 3.6. Each panel corresponds to a different subject with the red lines representing experimental data and the blue line representing model prediction. The dashed lines correspond to the condition in which the subject was not performing a task, while the solid line corresponds to the condition in which the subject was performing a task. The subject's self-reported MS data, along with the model predicted outputs for the on-road subjects are shown in Fig. 3.7. Among the eight subjects, five were male and three were female and their ages ranged from 21 to 71 years old. Tables 3.2 and 3.3 show the sum of residuals between model prediction and interpolated experimental data for each test condition defined as the following.

$$residual = \sum_{j=1}^{M} \sum_{i=1}^{N} ||MS_{model_{i,j}} - MS_{experimental_{i,j}}||$$

Table 3.2: Sum of residuals between MS model predictions and experimental data corresponding to Fig. 3.6 (scale of 10^4)

		A	**B**
Low Acceleration	**Task**	0.3087	2.0764
	No Task	0.8363	8.2187
		C	**D**
Moderate Acceleration	**Task**	6.8589	92.28
	No Task	0.7001	17.762

As observed in Fig. 3.6 and 3.7, the model has shown agreement with the trends observed for the experimental data. The same model parameters were used on the Mcity routes and

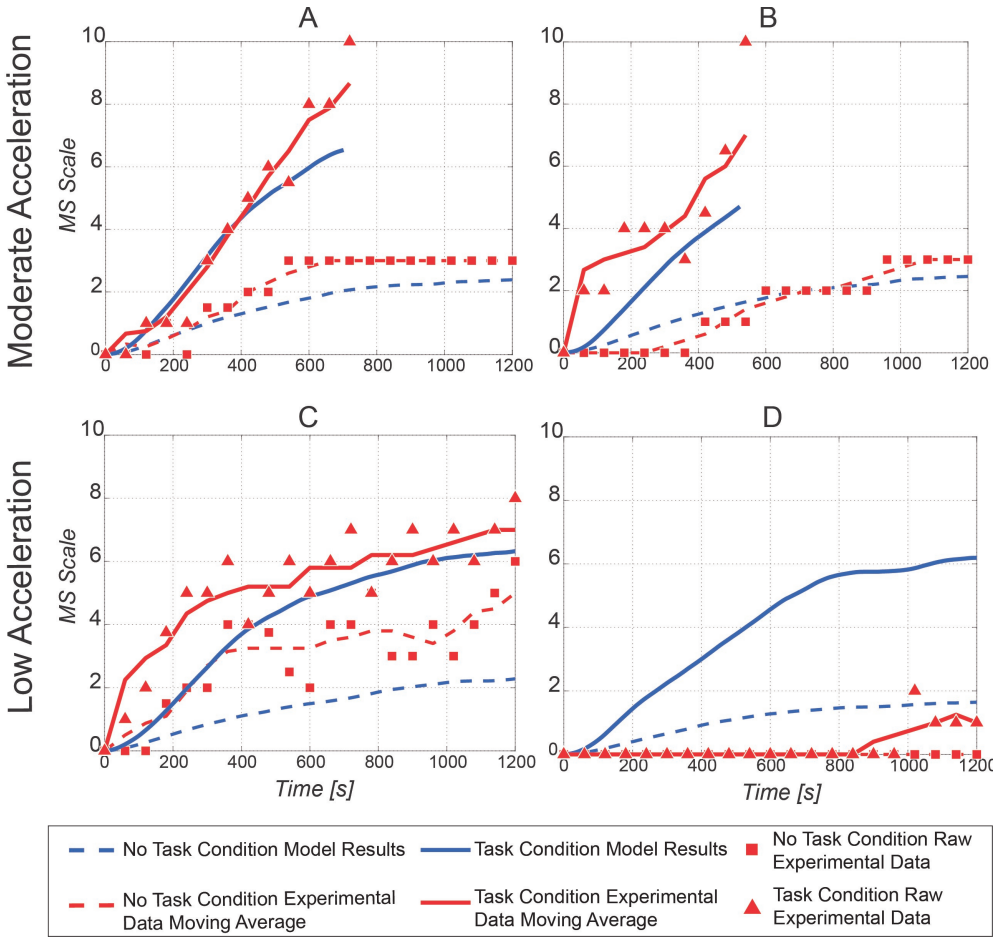


Figure 3.6: Experimentally measured and model predicted responses for passenger motion sickness during experimental runs performed at Mcity under low and moderate vehicle acceleration profiles from Jones et al [2]. Each subfigure shows a different subject.

on-road routes. Further, the same model parameters were used across different subjects. Despite changes in route and task conditions and individual subject differences, the model was able to capture the general trends observed for motion sickness response. Both Mcity routes and road routes showed comparable results in terms of the sum of residuals (within 1 order of magnitude) between model prediction and experimental data, indicating robustness of the model across different test paths. Further, both task and no task conditions showed comparable results in terms of the sum of residuals (within 1 order of magnitude), showing robustness of the model across different task test conditions. While this result indicates generalizability of the model, further analysis encompassing more subjects is still required.

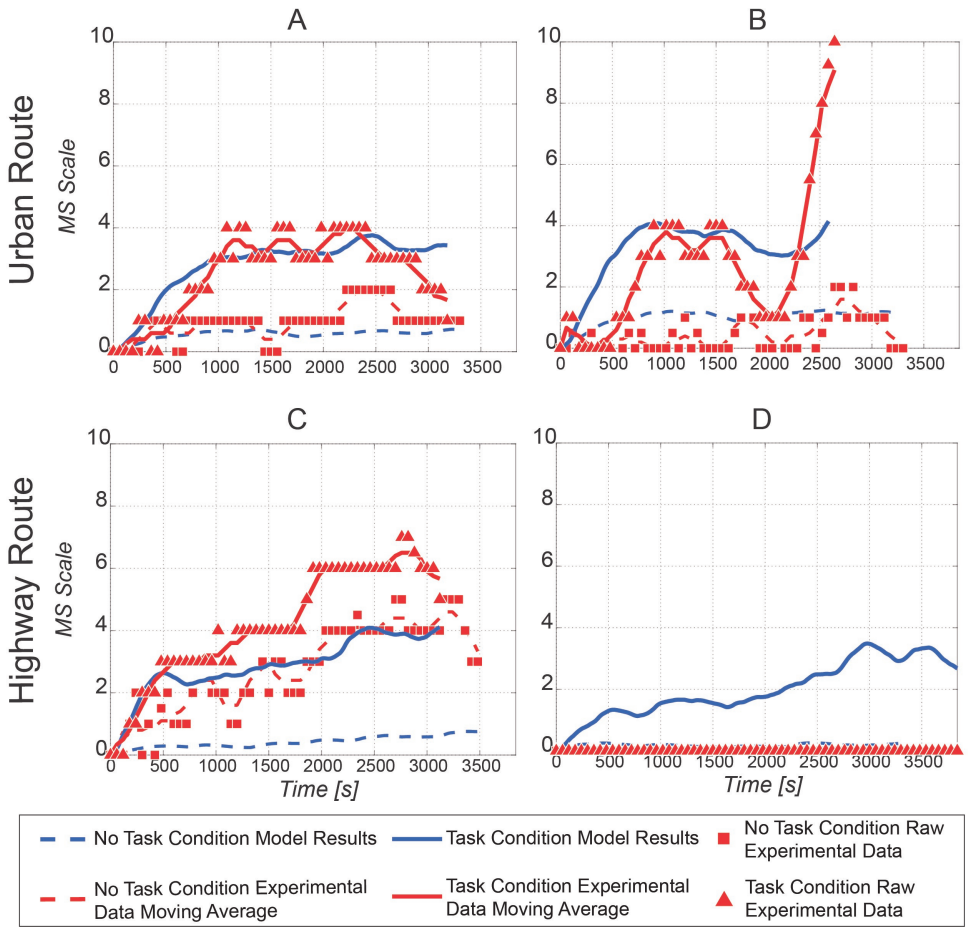


Figure 3.7: Experimentally measured and model predicted responses for passenger motion sickness during experimental runs performed during on-road conditions from Jones et al [2]. Each subfigure shows a different subject.

Due to the limited number of subjects available, a statistical analysis of the model results does not allow for conclusive results. This warrants further data collection and statistical analysis of the same.

Importantly, individual subjects have different levels of motion sickness susceptibility and subsequent motion sickness responses, which can cause deviation between model prediction and observed response. This can be observed for instance in Fig. 3.6.D and Fig. 3.7.D, where the subjects did not become motion sick despite exposure to routes that caused other subjects to become motion sick. To accurately estimate MS for each subject, individual characteristics must be taken into account. The proposed model doesn't account for other

Table 3.3: Sum of residuals between MS model predictions and experimental data corresponding to Fig. 3.7 (scale of 10^4)

		A	**B**
Urban Route	**Task**	2.4482	12.598
	No Task	2.2239	18.835
		C	**D**
Highway Route	**Task**	17.653	35.884
	No Task	29.836	1.2817

sources of variability that may influence passenger motion sickness response. These include, for instance, a passenger's motion sickness susceptibility, age, health condition (i.e., vestibular disease and migraine), physical (i.e., nutrition, sleep) and mental (i.e., stress) states, among the other factors associated with motion sickness. Subjects' behavior and posture during the test conditions are also hypothesized to influence the manifestation of MS symptoms. In the future, the model can be further parameterized and tuned to represent the variance in the population and provide the more accurate MS prediction given a subject's MS susceptibility. A model that accounts for population heterogeneity will enable the identification and evaluation of MS mitigation interventions that can potentially be implemented to improve passenger comfort on an individual basis. While the model parameters can be tuned to fit individual subjects' data, the goal of this study was to create a model that is generalizable across multiple subjects. With this, it's possible to use the MS model to provide an initial estimate of individuals who will become motion sick for a given acceleration exposure and task condition. This allows for the simulation of MS mitigation interventions that can potentially be implemented to improve passenger comfort.

Finally, the resolution of acceleration and angular velocity reference frames based on the subject's initial resting head posture introduces uncertainty as this head frame might

not be perfectly aligned with their vestibular and/or visual systems. While these systems' orientations are fixed with respect to the head, the resolution of IMU data on their frames might introduce alignment errors. Despite these limitations, the model was able to replicate the general trend observed for passenger motion sickness response.

While the subjective vertical conflict model proposed by Kamiji et al. was originally built to provide congruent results with motion simulator data in the MSI scale, we showed that the integrated SVC and human motion perception model proposed in this paper can be tuned to yield congruent results in different scales and driving and task conditions. This indicates that the proposed model is a fundamental step towards designing MS mitigation interventions that attempt to modulate the subject motion dynamics. In the future, the model's effectiveness on assessing MS mitigation can be further investigated to determine the extent to which the model can be used to design MS intervention systems.

3.3 Conclusion & Future Work

A model to predict motion sickness (VVMS) due to linear acceleration and angular velocity visual-vestibular stimuli in three dimensions was proposed along with a comparison of the model results with respect to experimental datasets. The model showed an improvement in MS prediction with respect to motion simulator MS triggering events under a visual-vestibular conflict condition when compared against the previous existing model proposed by Kamiji [82]. The model also showed congruent results when compared to realistic driving and task conditions from dataset captured from a larger investigation conducted by Jones et al [2]. In the future, the model can be further investigated in terms of its effectiveness in informing MS mitigating interventions. This would allow for the use of this model to design motion modulating interventions to improve passenger comfort. Further, characterization of the visual inputs can be implemented to predict MS under multiple in-vehicle scenarios. For instance, the model can be used for designing passenger interactions and experience inside

autonomous vehicles. As part of future research, the VVMS model can be combined with multibody dynamics simulation models which can simulate vehicle and passenger motion dynamics thereby allowing for the creation of an end-to-end motion sickness prediction that can simulate vehicle route, vehicle motion, passenger motion, and passenger performing tasks in the vehicle.

Further, the characterization of the visual flow beyond a binary configuration (no conflict vs full conflict) can be explored to improve the model's applicability to use cases where the subject might have a partially obstructed field of view. Further, the model proposed is not able to differentiate between individual subject characteristics. This is due to the nature of the uncertainty regarding the characterization of model parameters as a function of human variability. This limitation motivates the need for data-driven models for MS, which can take into account subject demographics for model prediction. The next chapters describe the data acquisition and model development processes to achieve accurate MS prediction.

CHAPTER 4

Experimental Protocol for Collection of On-Road Motion Sickness Data when Passengers Are Performing Tasks and Exposed to Preemptive Haptic Stimuli

The development of machine learning models warrants the availability of data for training and testing. The quantity and quality of available data can pose constraints on model performance and generalizability. In order to obtain data for the development of MS prediction models, a study was conducted to collect MS response data from on-road human subject trials at the Mcity test facility. While the experimental design falls outside the scope of this thesis, it is presented here briefly to provide context for the data used to build the models proposed. The models presented in the subsequent sections of this thesis were trained and tested in the dataset collected by the study described in Jalgaonkar et al [15, 83]. Below, a brief description of the study protocols is provided. For further details on the experimental work, refer to [15].

For each trial in this experiment, subjects were driven inside the cargo area of a modified Ram Promaster van through 3 loops of a test track for a total of approximately 22 minutes. The subjects had no view of the outside world or the driver area, creating a 'Wizard of Oz' setup. The subjects were instrumented with multiple sensors and were requested to report

their MS score every 90 seconds during their trial. Figure 4.1 shows the test vehicle, and Figure 4.2 shows the test track used for this experiment [15].

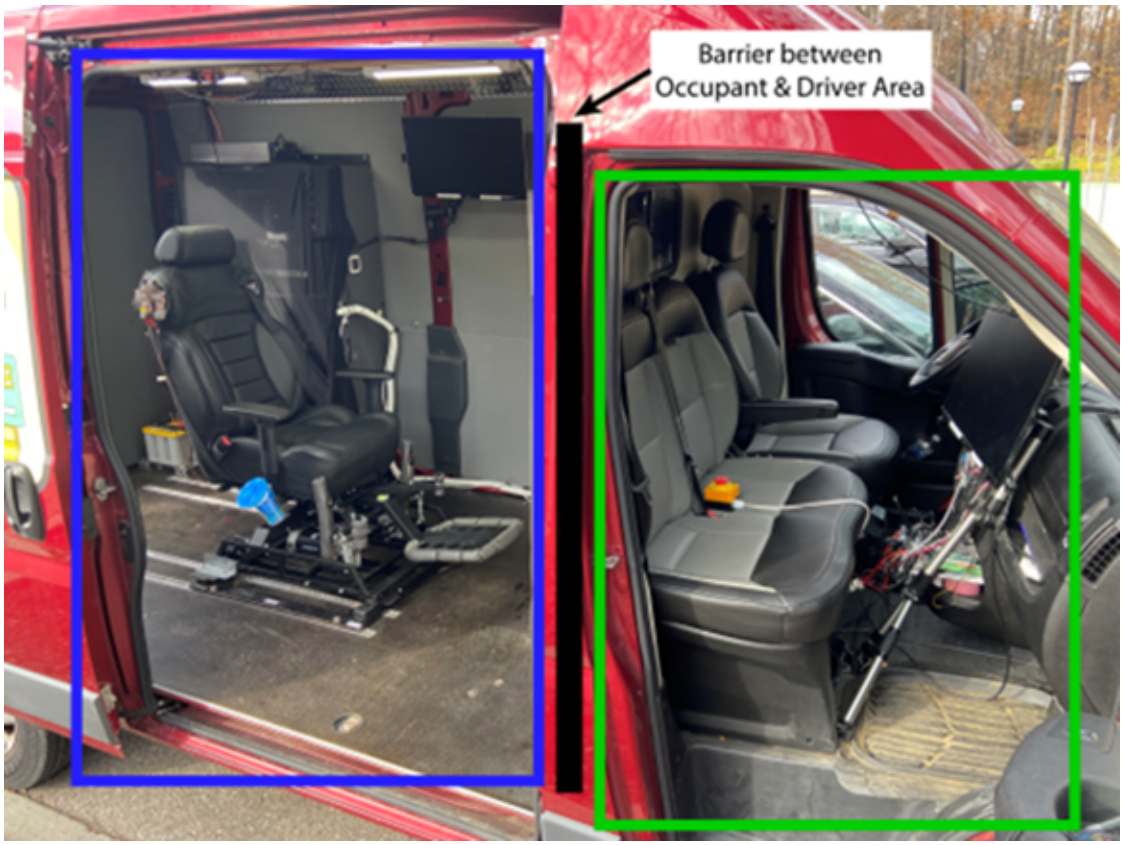


Figure 4.1: Vehicle platform built for subject trials

The experiment included two independent variables: haptic stimuli system (HSS) and representative productive task. The different test conditions for this study are shown in Table 4.1. The 'On' state for the haptic stimuli system variable indicates that vibrotactile motors embedded in the seat were actuated 3s ahead of a turn or break event to preemptively alert the passenger of upcoming vehicle maneuvers. The 'On' state for the task variable indicates that the passenger performed cognitive tasks on a tablet during vehicle motion. A total of 35 subjects participated in the study, with 24 of them completing all 3 test conditions. Subjects that did not complete all test conditions were still taken into account for modeling purposes.

This study used a numerical motion sickness reporting scale that was based on the previ-

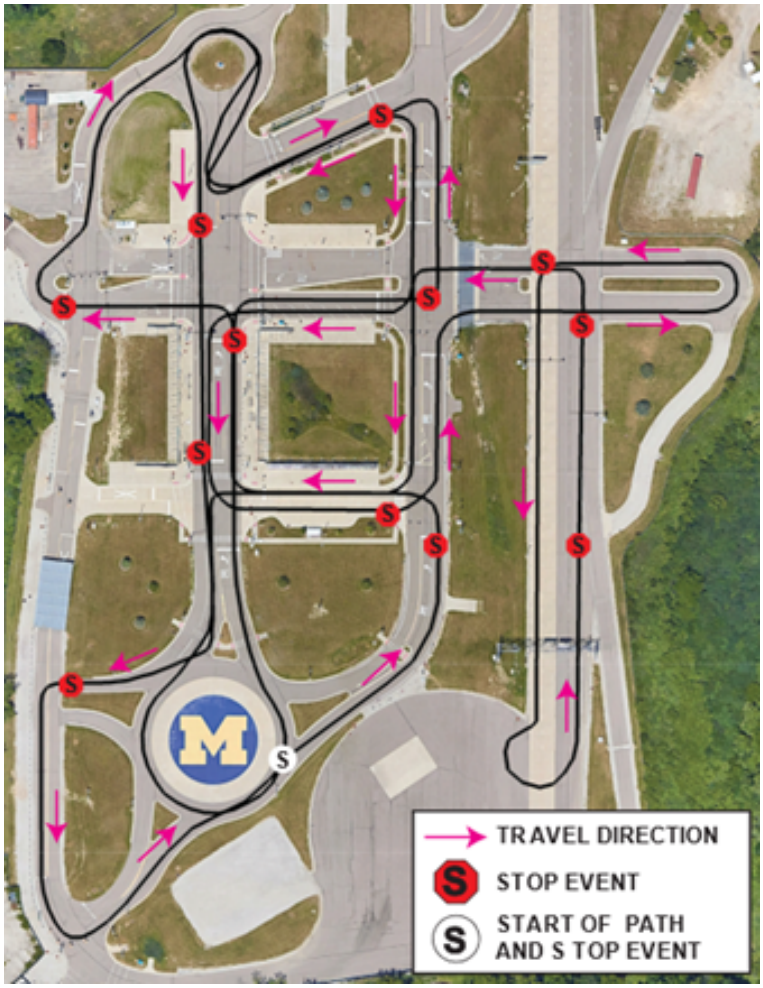


Figure 4.2: Mcity test track and designed path to conduct on-road data collection

ously developed University of Michigan Transportation Research Institute (UMTRI) Motion Sickness Scale [2]. The scale used ranges from 0 to 10, with 0 meaning that the subject has no motion sickness and 10 meaning that the subject needs to stop the trial as they are about to throw up. Subjects were provided with a visual aid in understanding the scale, as shown in Figure 4.3. The subject was informed that a score of 1-3 corresponds to low MS intensity, 4-7 corresponds to medium MS intensity and 8-10 corresponds to high MS intensity. Further, subjects were made aware that MS arises as a combination of symptoms and they were informed of the nature of such symptoms (Table 4.2). They were asked to report their best estimate for their MS score considering the intensity of the combination of symptoms they experienced. At the beginning of the trial, the onboard researcher asked the

Table 4.1: Test conditions and independent variables

Test Condition	**Haptic Stimuli System (HSS)**	**Task**
TC1	ON	OFF
TC2	OFF	ON
TC3	ON	ON

subjects to report their motion sickness score before the vehicle started moving. Once the vehicle started moving, the researcher was instructed to start a timer and ask the subject for their MS score every 90 seconds.

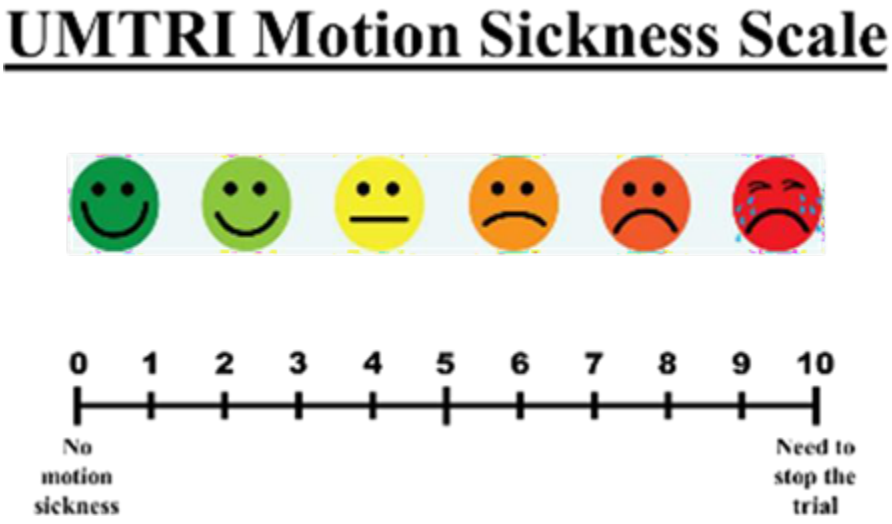


Figure 4.3: UMTRI Motion Sickness Scale with smiley face visual aids that can be shown to study participants

A Delsys Trigno Avanti wireless system was used for acquiring and logging sEMG data. The Delsys Trigno Avanti EMG+IMU wireless sensors were used for collecting data from 2 muscles of each subject, the left sternocleidomastoid, and the right sternocleidomastoid muscles. The location of the sternocleidomastoid sensors is shown in Figure 4.4. Appropriate measures were taken to ensure that the sEMG sensor was properly aligned with the muscle

Table 4.2: Common symptoms and sensations associated with Motion Sickness

Sensation Group	**Examples**
Discomfort felt at the head	Sensations can include tension or pressure, fogginess, a fullness of the head, headaches, changes in mood, irritability, eye strain
Body temperature changes	Sensations of being very warm or cold, feeling of body warmth, excessive sweating, cold sweats
Drowsiness	Yawning, shortness of breath or heavy breathing, feeling of haze or drowsiness, fatigued, inability to concentrate or focus
Dizziness	Lightheaded-ness, feeling shaky, disoriented, sense of spinning, dizziness with eyes open/eyes closed, whirling, tilting, rocking, falling or motion, imbalance
Unpleasant feelings in the mouth	Sensations can include increased salivation or drooling, dry mouth, burping
Discomfort felt at the stomach	Sensations include general nausea, feeling ill or uneasy, hypersensitivity and awareness of stomach movements, queasiness, feeling like imminent vomiting or vomiting, feeling bloated
Others	Any sensation that is abnormal or atypical leading to feeling unpleasant

fibers and that they had good contact with the skin surface. The researcher verified that data collection was operational by asking the subject to move each of the muscles of interest and observing the live data feed to ensure the muscle movement was being recorded. The sEMG data was logged using the EMGworks software at a rate of 2kHz. The Delsys Trigger Module was used to automate the start and end of data logging with the rest of the data logging systems. The data collection trigger time was used to synchronize the sEMG data with the MS score.

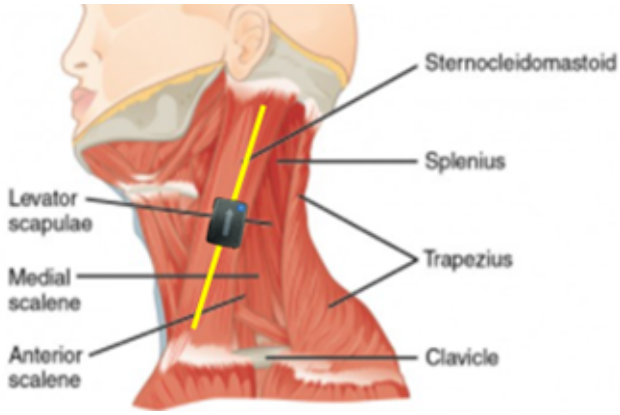


Figure 4.4: Placement of sEMG sensors on the sternocleidomastoid muscle

An ICM2948 IMU sensor was placed on the subject's forehead using a headband as shown in Figure 4.5. The sensor was configured to capture two vectors, angular velocity, and linear acceleration, across three axes, representing the six degrees of freedom, and the data was sampled at a frequency of 100 Hz. An Empatica E4 wristband was used to collect blood volume pulse (BVP) at 64Hz and electrodermal activity (EDA) data at 4Hz. The E4 wristband is shown in Figure 4.6 alongside the full suite of sensors used for collecting subject data.



Figure 4.5: Head IMU sensor placement

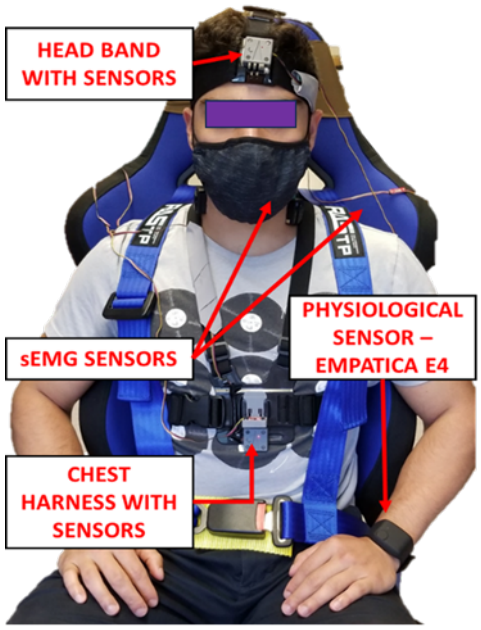


Figure 4.6: Sensor suite used during experimental protocol

After the subject was seated inside the vehicle platform and data acquisition was initiated, 90 seconds of baseline data were collected during which the subject was instructed to remain static and to maintain an upright posture. After baseline data was collected, the vehicle proceeded to the beginning of the test track, where the trial started. After the trial was completed, the vehicle returned to the office building and the data collection process ended. The timeline describing this process is shown in Figure 4.7. All data processing techniques used in the following sections required appropriate cropping of the data signals according to the data acquisition timeline presented.

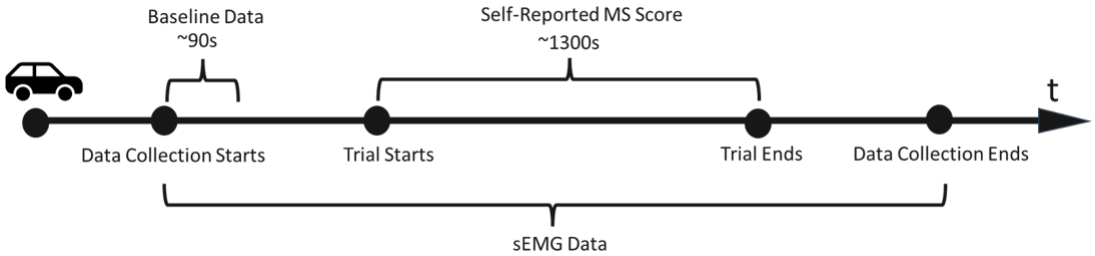


Figure 4.7: Timeline for data collection process within the context of the experimental trial

The experiment protocol discussed here yielded one of the most extensive MS datasets in

the literature. This enabled the development of machine learning models that can leverage both dynamic and static data to make predictions. The inclusion of a test condition that attempts to mitigate motion sickness, the presence of cognitive tasks, and the relatively extensive dataset size enables the development of these models with the goal of real-world implementation for the design of motion sickness mitigation technology. The subsequent sections describe the process by which this dataset was leveraged for the creation of MS prediction models. While this dataset is relatively extensive when considered within the context of MS experiments, it can still be scaled further. For instance, the recruitment of subjects of broader age groups and the expansion of data collection for MS response in the high-intensity category are elements that can compromise model performance for specific use cases.

CHAPTER 5

Data-Driven Prediction of Car Sickness Using Head Motion and Time Series Feature Engineering Methods

The previous Chapter outlined the data collection process used to build the dataset with the goal of training the machine learning models. In this Chapter, the process describing the data preprocessing and model implementation is presented within the use case of head motion data. Classification and regression model pipelines are proposed for predicting MS response as a function of head motion data collected through the IMU sensor placed on the subject's forehead.

5.1 Data Preprocessing

Among the data collected for all trials, only 55 trials meeting the minimum duration criterion of three time steps (>270 seconds) with valid IMU data were included in the analysis. That means that if a sensor got disconnected before the 270s mark, the entire trial was removed from consideration. Figure 5.1 shows the overall model architecture used for MS prediction, with data preprocessing as the first step in this pipeline.

A static vector was introduced to distinguish between individual trials and improve the model's predictive accuracy. This static vector was conjugated with three components $[H_P]$,

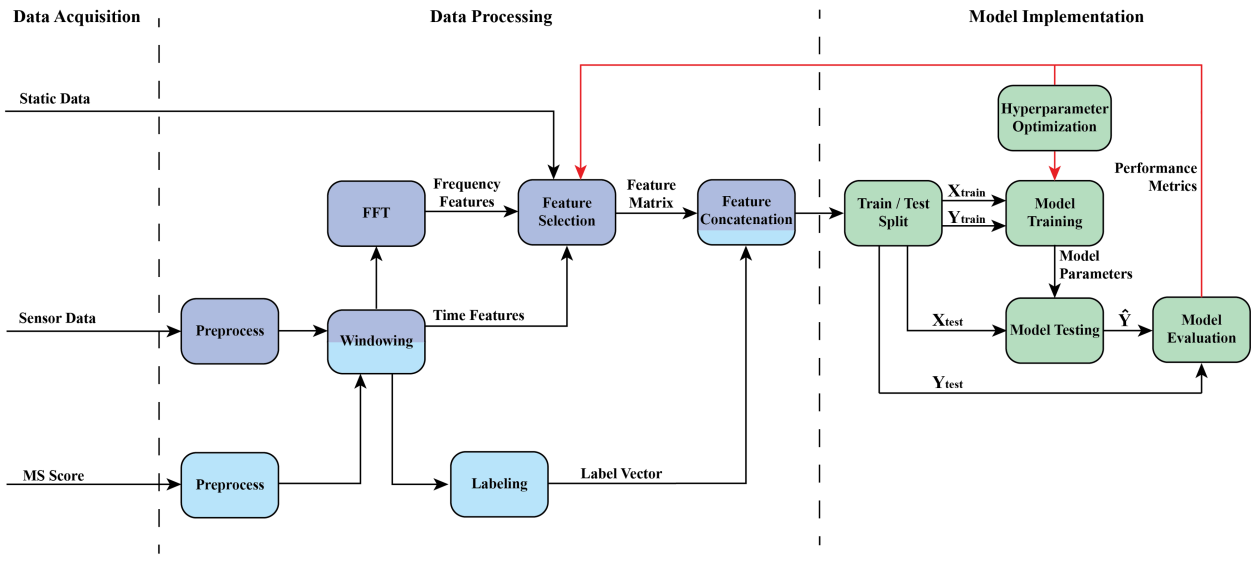


Figure 5.1: MS Prediction Model Architecture

$[T_P]$, and $[S_P]$, as defined in Table 5.1. The demographics were integrated with $[H_P]$, whereas the experimental conditions, which include the task type and state of HSS, were defined with $[T_P]$ and $[S_P]$. Ultimately, the input vector for the predictive model $[E_F]$ was constructed by integrating the dynamic features of the IMU head data with the static vector components.

In order to generate the dynamic features of the IMU head data, the signal was subjected to a bandpass filter with cutoff frequencies of [0.03, 5] Hz. The high-pass filter at 0.03 Hz was employed to eliminate DC content. The low-pass filter at 5 Hz was applied to remove the noise and retain the frequency spectra relevant to the onset of MS, which has been identified as 0-2Hz by McCauley et al[55]. Subsequently, twenty-seven features (Table 5.2) of the IMU head data, derived from each of the six vectors, were computed for each ninety-second window, aligning the dataset with the time steps of the recorded MS scores.

To reduce data dimensionality and computational complexity, only the most effective features in the frequency and time domains were deduced for the regression and classification approaches. For each of the six data streams corresponding to the IMU degrees of freedom, the most relevant features were identified for modeling using a predictor importance analysis based on the Gini coefficient [73]. The best nine features of each data stream were selected

for regression modeling. These features were selected to represent the IMU head data over the ninety-second time window to match the sampling rate of the MS scores. While this feature analysis doesn't provide a direct measure of the contribution of each feature in terms of model accuracy, it allows for the model to obtain high prediction performance by avoiding performance degradations due to high-dimensional datasets. This does not guarantee that each feature is substantially contributing to model performance, but it provides an effective method to ensure that the model performs well for the available features and data points. Future optimization can be employed to remove redundant features with the goal of decreasing computational time.

The subsequent section discusses the detailed steps for developing predictive models based on regression and classification techniques.

Table 5.2: Definition of IMU head data dynamic features

Property	**Description**
Frequency Domain	
Mean Frequency	$MNF = \frac{\sum_{l=1}^{M} f_l p_l}{\sum_{l=1}^{M} p_l}$ Where f_l is the spectral frequency in the bin of frequency l, p_l is the EMG signal power spectrum in the bin l, and M is the frequency bin length.
Median Frequency	$\sum_{l=1}^{MDF} P_l = \sum_{l=MDF}^{M} P_l$ It is the frequency divided into two regions with the same amplitude; that is to say, MDF is the total power average and could be expressed as the number MDF with the property where P_l is the EMG signal power spectrum at a frequency bin l, and M is the frequency bin length.
Peak Frequency	$PKF = (p_l)$
Mean Power	$MNP = \frac{\sum_{l=1}^{M} p_l}{M}$

Total Power	$TTP = \sum_{l=1}^{M} P_l$
Frequency Ratio	$FR = \frac{\sum_{l=LLC}^{ULC} p_l}{\sum_{l=LHC}^{UHC} p_l}$, Where ULC and LLC are upper and lower coefficients of the cutoff frequency of the low band frequency and UHC and LHC are those from the high frequency, respectively.
Power Spectrum Ratio	$PSR = \frac{P_0}{P}$ where $P_0 = \sum_{l=f_0-n}^{f_0+n} P_l$ and $P = \sum_{l=-\infty}^{\infty} P_l$ with f_0 the PKF value and n a hyperparameter.
Power Spectral Density	$PSD(f) = \lvert X(f)\rvert^2$ where X is the Fourier Transform.
Frequency Mean Density	$FMN(f) = \frac{\sum_{i=1}^{M} f_i PSD_i}{\sum_{i=1}^{M} PSD_i}$
Frequency Median Density	$FMD(f) = \frac{1}{2}\sum_{i=1}^{M} PSD_i$
Time Domain	
Average Amplitude Value	$AAV = \frac{1}{N}\sum_{k=1}^{N} x_k$
Mean Absolute Value	$MAV = \frac{1}{N}\sum_{k=1}^{N} \lvert x_k\rvert$
Modified Mean Absolute Value	$MMAV = \frac{1}{N}\sum_{k=1}^{N} w_k \lvert x_k\rvert$ where $f(x) = x$ if $x > 0$ else 0.
Variance	$VAR = \frac{1}{N-1}\sum_{k=1}^{N} x_k^2$
Zero Crossings	ZC is the count of the zero crossings for the signal.

Average Amplitude Change	$AAC = \frac{1}{N}\sum_{k=1}^{N} \lvert x_{k+1} - x_k \rvert$
Simple Square Integral	$SSI = \sum_{k=1}^{N} x_k^2$
Slope Sign Changes	$SSC = \sum_{i}^{n} f_{ssc}(x_i), \quad f_{ssc} = \begin{cases} 1, & \text{if } x_i < x_{i+1} \text{ and } x_i < x_{i-1} \\ 1, & \text{or } x_i > x_{i+1} \text{ and } x_i > x_{i-1} \\ 0, & \text{otherwise} \end{cases}$ This feature allows another description of the frequency; it is the number of times that a slope sign changes occur.
Waveform Length	$WL = \sum_{k=1}^{N} \lvert x_k - x_{k-1} \rvert$ WL is the accumulated waveform length above the time segment.
Wilson Amplitude	$WAMP = \sum_{k=1}^{N-1} f(\lvert x_{k+1} - x_k \rvert)$

In addition, an analysis was performed to determine the correlation between time and frequency domain features for the head motion data, as shown in Figures 5.2 and 5.3. The heat map illustrates the intercorrelation between features used, and identifies some of those features as highly correlated. The use of correlated features can lead to unnecessary increased dimensionality, which can compromise performance for models that struggle in high-dimensional spaces, such as SVM. The described feature importance selection method helps offset the observed redundancy, leading to decreased dimensionality for these models. While this method does not explicitly remove intercorrelated features, it reduces the number of features that do not contribute to improved model performance, thereby decreasing the overall number of intercorrelated features.

The feature importance analysis results are shown in Tables 5.3 and 5.4. Table 5.3 shows the importance of each of the six head motion data streams as an average of the importance for all the features extracted. Lateral, longitudinal, and vertical linear acceleration

Table 5.1: Static features considered for model prediction

Static Variables	**Magnitudes**		
H_P	[gender, susceptibility, age]		
S_P	[HSS active, HSS inactive]		
T_P	[task, no task]		
Age distribution	Females: [19 31]; Males: [19 34]		
Gender distribution	12 Females, 9 Males		
Trial distribution	30 Female, 25 Male		
Susceptibility index	Low [1]; Medium [2]; High [3]		
Gender (M/F)	Male (2)	Female (1)	
Test conditions (TC)	(TC1) [HSS active, No Task]	(TC2) [HSS inactive, Task]	(TC3) [HSS active, Task]
Three test cases	5 participants (2 Females, 3 Males)		
Two test cases	17 participants (10 Females, 7 Males)		
One test cases	6 participants (4 Females, 2 Males)		

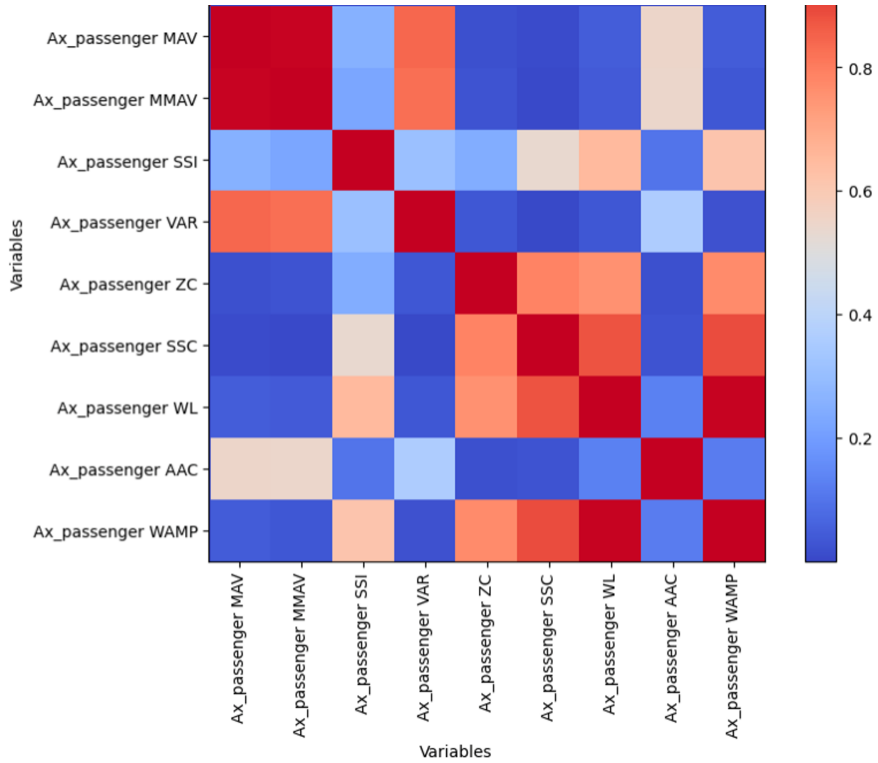


Figure 5.2: Correlation analysis for time-based head IMU features

were identified as the most important data streams for MS prediction, in this order. This underscores the key role of the otolith sensor within the brain's mechanisms that lead to MS. However, the vertical acceleration stream shares similar importance when compared to the angular velocity streams, indicating that the inclusion of angular velocity for modeling purposes is still paramount for accurate predictions. Table 5.3 shows the importance of each feature extracted as an average across all data streams. The Slope Sign Changes (SSC), the Mean Absolute Value (MAV), and the Zero Crossings (ZC) were identified as the most important features. This finding underscores the importance of the magnitude and oscillatory behavior of head motion for MS prediction.

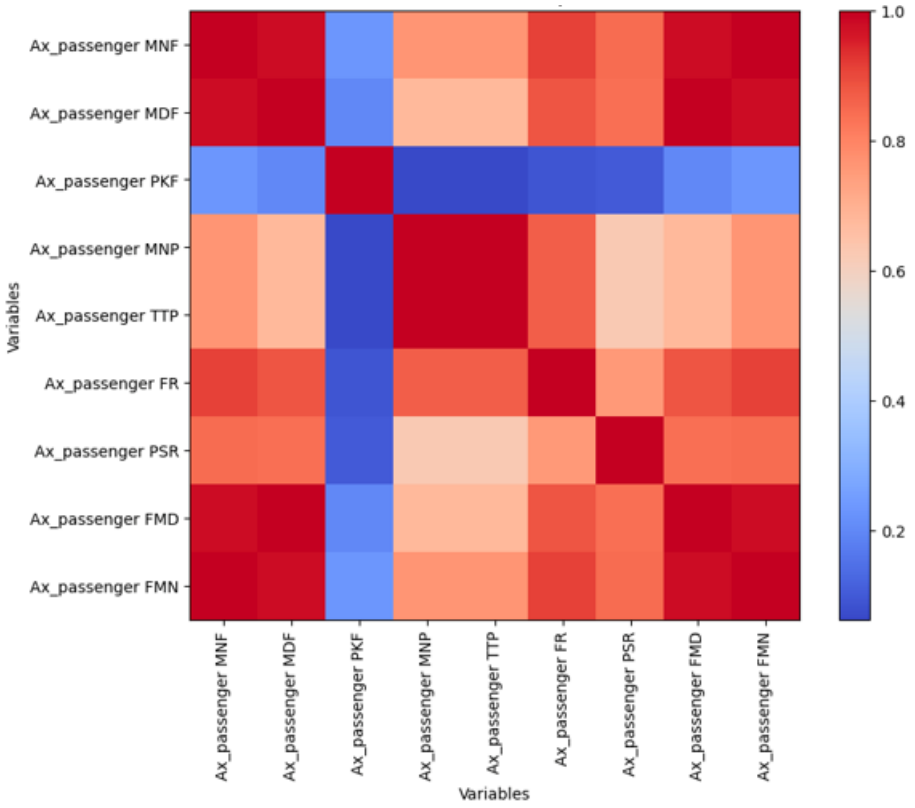


Figure 5.3: Correlation analysis for frequency-based head IMU features

5.2 Predictive Modeling

5.2.1 Regression

Given that both the IMU data and MS score were extracted in the time domain, the proposed framework investigated the use of the most established time-series deep learning predictive models, Nonlinear Autoregressive Exogenous (NARX) Dynamic Neural Network (DNN) and Long Short-Term Memory (LSTM) Recurrent Neural Network (RNN) [35][84][85][86]. NARX was chosen as one of the most prominent frameworks as it can predict future MS score output values based on previous outputs and exogenous inputs from head IMU data. Conversely, the LSTM network was considered since it can account for MS scores' long- and short-term dependencies on the dynamic state of the head. The detailed list of solvers and training functions is presented in Tables 5.5 and 5.6.

Table 5.3: Relative importance of head motion data streams calculated using the Gini index

Data Stream	**Importance**
A_x	29.95
A_y	15.06
A_z	14.74
G_x	14.65
G_y	12.22
G_z	11.69

The performance of 21 models - comprising 12 NARX and 9 LSTM networks - has been evaluated in the existing literature to determine the most effective solver and layer configuration for mapping vehicle IMU data to MS scores [35]. The findings indicate that the "trainrp" solver for NARX and the "gru" layer for LSTM yield optimal results while minimizing computational time. Consequently, this study employs the same solvers to map head IMU data to MS scores. Furthermore, the "adam" solver was selected for LSTM modeling alongside the "gru" layer due to its ability to integrate the benefits of adaptive gradient and root mean square propagation techniques, thereby dynamically adjusting learning rates during training.

The parameters used for the deep learning models are included in Tables 5.8 and 5.7, and the strategy deployed is outlined in Figure 5.4. As discussed in the preceding section, the dataset consisted of 55 trials, and the following steps were undertaken to predict the output: (Step 1) One trial was isolated, while 37 trials (66%) were randomly selected from the remaining 54 trials. (Step 2) The 37 trials were used to develop the training functions, applying the default split strategy (70% training, 15% validation, 15% testing). (Step 3) After validation, the NARX model was transitioned from an open-loop to a closed-loop

Table 5.4: Relative importance of head motion features calculated using the Gini index

Feature	**Importance**
SSC	16.31
MAV	9.31
ZC	6.19
SSI	5.29
TTP	5.18
PSR	5.15
MNP	5.09
PKF	5.03
MNF	4.85
FMN	4.84
MMAV	4.61
FMD	4.43
AAV	4.28
MDF	4.16
AAC	4.05
WL	4.03
FR	3.82
WAMP	3.14
VAR	3.13

Table 5.5: NARX solvers and training functions

NARX Model solvers	
Solvers	**Training Function**
'trainlm'	Levenberg-Marquardt
'trainbr'	Bayesian Regularization
'trainbfg'	BFGS Quasi-Newton
'trainrp'	Resilient Backpropagation
'trainscg'	Scaled Conjugate Gradient
'traincgb'	Conjugate Gradient with Powell/Beale Restarts
'traincgf'	Fletcher-Powell Conjugate Gradient
'traincgp'	Polak-RiDbiére Conjugate Gradient
'trainoss'	One Step Secant
'traingdx'	Variable Learning Rate Gradient Descent
'traingdm'	Gradient Descent with Momentum
'traingd'	Gradient Descent

Table 5.6: LSTM solvers and layers

LSTM Model solvers	
Layers	**Properties**
LSTM	Learns long-term dependencies between steps
bi-LSTM	Learns bi-directional long-term dependencies
GRU	Learns short-term dependencies between steps
Solvers	**Definition**
sgdm	Stochastic gradient descent with momentum
rmsprop	Root mean square propagation
adam	Adaptive moment estimation

structure, a process not applicable to LSTM. (Step 4) The isolated trial from Step 1 was then input into the trained models to predict the MS score. (Step 5) Steps 1-4 were repeated ten times, and the Root Mean Square Error (RMSE) values were computed for the Error vector (actual MS score vs. predicted MS score) and its first-order derivative (dError). The comparative performance of both models is analyzed in the subsequent sections.

5.2.2 Classification

Classifying motion sickness (MS) into discrete categories enhances the capability of machine learning models to assess the passenger's condition while consistently providing interpretable output. This strategy segments MS into well-defined classes, making predictive modeling simpler and faster than the continuous score estimation required in regression. Three machine-learning algorithms were implemented for this classification approach: Support Vector Machine (SVM), Random Forest, and XGBoost [87]. The parameters and configurations for these models are detailed in Table 5.9.

Table 5.7: LSTM model parameters

LSTM Model Parameters	
Solvers	adam
Max epochs	2, 20
Gradient Threshold	1
Initial learning rate	0.05
Hidden Units	200
Layer 1	Sequence Input
Network Layer	GRU
Layer 3	Fully Connected
Layer 4	Regression Layer

Table 5.8: NARX model parameters

NARX Model Parameters	
Solver	trainrp
Input Delays	1:2
Feedback Delays	1:2
Hidden Layer Size	10
Network 1	Training - Open
Network 2	Validation - Closed
Dataset Analysis 1	[70% Training]
Dataset Analysis 2	[Validation 15%, Testing 15%]
Performance	Mean Squared Error

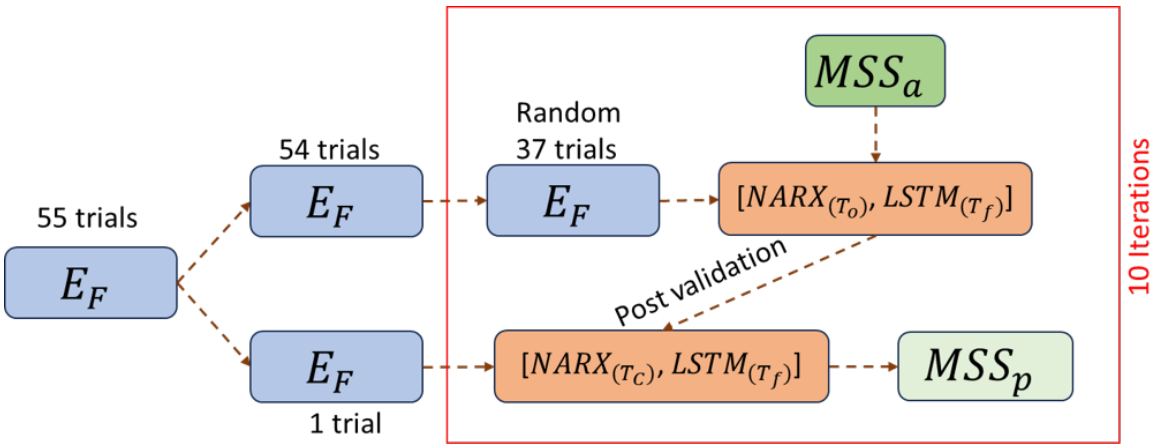


Figure 5.4: Regression prediction modeling and validation strategy

Table 5.9: SVM, XG Boost, and Random Forest model hyperparameters

SVM		**XG Boost**		**Random Forest**	
Kernel	RBF	Trees / Learning Rate	300 / 0.3	Number of Trees	300
Gamma	0.00001	Max Depth	10	Max Depth	None
C	100	Booster	GB Tree	Criterion	Gini

While the NARX and LSTM algorithms can handle data with variable input lengths, classification methods require the input data to have fixed dimensions. Consequently, two samples with different feature vector lengths could not be fed to the same model configuration, limiting the ability of the model to capture previous input data trends to make its predictions. Two unique methods of extracting data features were devised and evaluated to address this compatibility issue while retaining the temporal characteristics of MS throughout the ride. The first method, the expanding window technique, constructs two feature vectors: one representing the most recent 90-second data window and another summarizing all previous 90-second segments. The preceding feature vector is obtained by averaging feature values from time t=0 to t=n-1, where n indicates the current 90-seconds window index. The term expanding window reflects how the preceding feature vector includes more

historical data as the trial unfolds. Figure 5.5 shows an example of the application of the expanding feature method at n=4 for a trial with fifteen 90-second time windows.

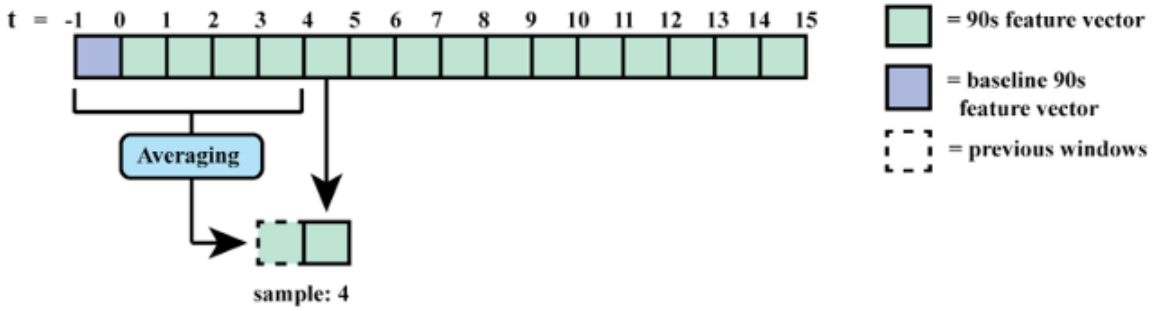


Figure 5.5: Classification expanding window feature engineering strategy

A second method was devised to accommodate feature vectors of different sizes, the time-offset approach. In this method, the lagging features are maintained as separate vectors instead of as an average of the features from past windows. Figure 5.6 shows the time-offset process used to generate the feature matrix from the time domain, frequency domain, and static data. For each trial, the feature matrix was created by stacking the feature vectors for each 90s time window such that each row corresponds to a time window and each column corresponds to a feature. Afterward, a copy of this feature matrix was generated and modified by shifting each feature vector downwards by one time step to create lagging features. This process was repeated for the number of chosen time offsets, and the resulting matrices were concatenated horizontally in chronological order. The feature matrix with time window offsets would lead to blank cells associated with the time shift of the feature vector from the previous time window. To preserve consistency in dimensionality, the cells that would be left blank were padded by inputting the feature vector extracted from the baseline data. Finally, the feature matrices for each trial were stacked vertically to yield the compiled feature matrix used for model implementation. This process was done so that the feature vector for a given time window includes the features corresponding to the trial's previous time windows. Since the incidence of MS is a cumulative phenomenon over time, data from the past is relevant for prediction, and this method allows the model to capture

the cumulative nature of that data while performing predictions for each time step. The number of previous time windows to include is an important hyperparameter in the model; the effect of this number of time steps on model performance is discussed in the results section.

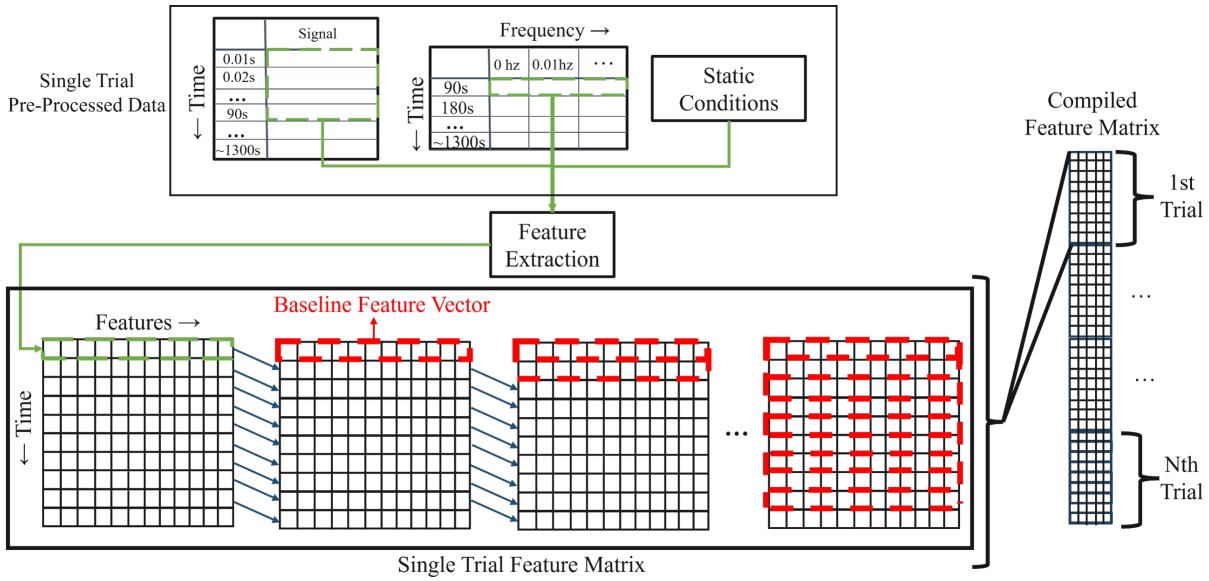


Figure 5.6: Classification time-offset feature engineering strategy

A third method for windowing was employed, using the current window to make predictions without accounting for past-time steps to serve as a benchmark for comparison purposes. The expanding window and time-offset techniques present trade-offs in input vector composition. The expanding window method reduces input dimensionality and consistently integrates data from the entire trial, but sacrifices granularity by averaging across all historical windows. Conversely, the time-offset method maintains temporal details by keeping separate previous windows but can significantly increase input dimensionality. Regardless of the feature extraction method, each input vector corresponds to a single output label representing an MS score classified into predefined categories. This study investigates binary and ternary classification schemes. In binary classification, MS scores between 0 and 2 are labeled low, while scores from 3 to 10 are labeled high. For ternary classification, scores of 0–1 are considered low, 2–4 as medium, and 5–10 as high. These thresholds were designed

to balance label distribution across the dataset and reflect the general ranges of MS intensity a passenger feels. The distribution of labels was defined to preserve a 50/50 distribution for binary classification and a 33/33/33 distribution for ternary classification. An unbalanced distribution of labels could generate bias in the model, leading it to predict one class more often than others based on recurring past observations.

The dataset was split by entire trials for testing and training, meaning all the samples from any particular trial were exclusively assigned to either the testing or training set. This measure was taken to maintain the integrity of the testing set by ensuring the model could not train on data from the same trial used for testing. Of the 55-trial dataset, 80% of trials were allocated for training and 20% for testing. A grid search with 5-fold cross-validation was used to determine the hyperparameters that maximized model robustness. A customized K-fold algorithm was used to ensure an even distribution of trials across training and validation sets. This K-fold method is described in Figure 5.7. The first step in the process described in Figure 5.7 was to group a given subject's trials and assign them a unique index, hereby defined as the subject index. Hence, a subject index grouped either one, two, or three trials depending on how many trials the subject participated in. The second step in this process was to randomly shuffle the groupings according to their subject index. After the subjects' indices were shuffled, the third step consisted of assigning each trial to alternating folds. This ensured that no two trials from the same subject were present in the validation set. For subjects with multiple trials, up to one trial was included in each fold. This process enhanced the diversity of validation data by maximizing the number of unique subjects represented in cross-validation, aiming to improve the model's generalizability. Maximizing data diversity is particularly crucial due to the dataset's relatively small size, as it helps to capture representative population patterns better. The fourth step was isolating a single fold for testing and using the remaining four folds for training. Finally, the fifth step consisted of repeating this process by isolating a different fold each time for five iterations.

For the SVM, the hyperparameters optimized included the gamma (decision boundary

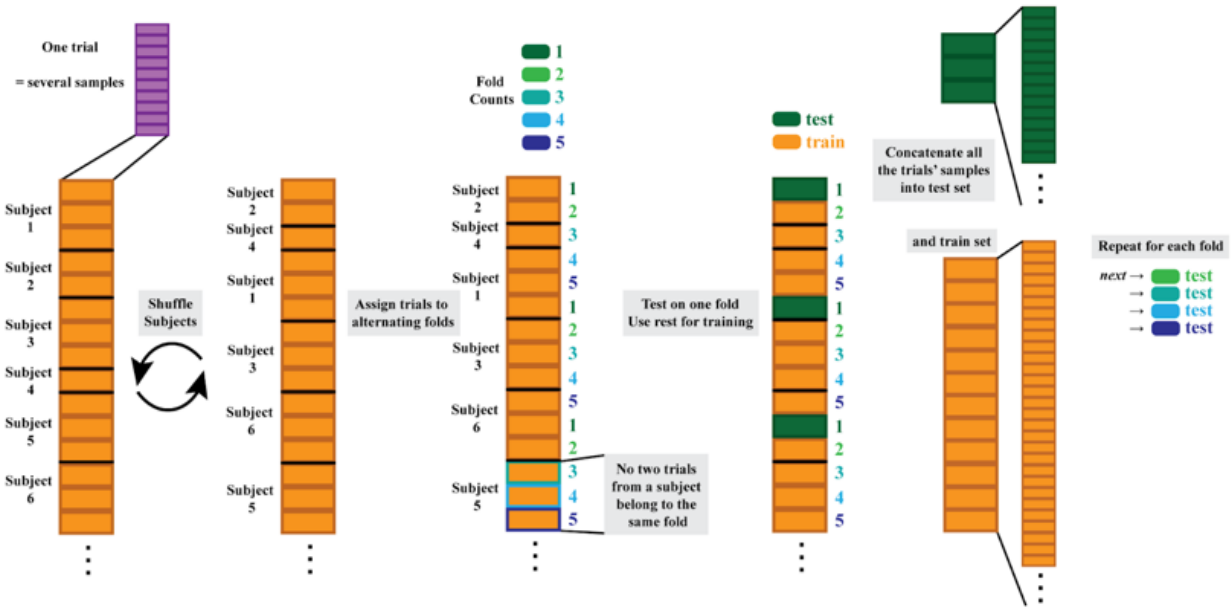


Figure 5.7: Custom K-fold validation used for classification

smoothing) and C (regularization) parameters; for the Random Forest, the tree-splitting criterion and number of trees; and for XGBoost, the maximum tree depth and number of trees. Feature selection employed K-fold cross-validation, with Gini importance calculated over 100 iterations for decision tree models to assess feature contributions. While Random Forest and XGBoost performed best using the complete feature set, SVM, which is susceptible to overfitting in high-dimensional spaces, required a reduced feature set. The top five features were selected for the SVM feature set based on the Gini analysis. Additionally, the best combination of three frequency domain and three time domain features was determined via brute force cross-validation. These six features were further incorporated into the SVM feature set for a final total of 11 features used for modeling.

5.3 Results

The first modeling approach of this study deployed a regression approach with deep learning models to predict the MS score. The NARX and LSTM regression models were tested for

Table 5.10: Statistical analysis of LSTM Regression Model performance

RMSE statistics - LSTM [GRU, ADAM]

Time (s)	1447.75			
Vector	Minimum	Maximum	Mean	Deviation
Error	0.758	4.484	2.338	0.762
dError	0.308	2.476	0.958	0.354

Table 5.11: Statistical analysis of NARX Regression Model performance

RMSE statistics - NARX [Train RP]

Time (s)	664.557			
Vector	Minimum	Maximum	Mean	Deviation
Error	0.309	5.443	2.069	1.027
dError	0.170	2.078	0.683	0.317

each trial across ten iterations. Tables 5.10 and 5.11 present the LSTM and NARX models' performance, respectively. These tables include the training computational time and the RMSE statistical values calculated across all trials and iterations. Further, Figure 7 shows sample predictions for each model alongside the true data labels.

The second modeling approach of this study deployed three algorithms to predict MS scores in binary and ternary classes, including SVM, Random Forest, and XG Boost. The metrics used to evaluate the models' performance consist of accuracy, F1 score, and AUC. Different feature extraction methods, including expanding window, time offset, and current window methods, were assessed individually. Table 5.12 details binary classification performance analysis as a function of the model and feature extraction method. Table 5.13 showcases the performance metrics for the best-performing binary and ternary classification models across different models. Figure 5.9 shows the confusion matrix for the best-performing

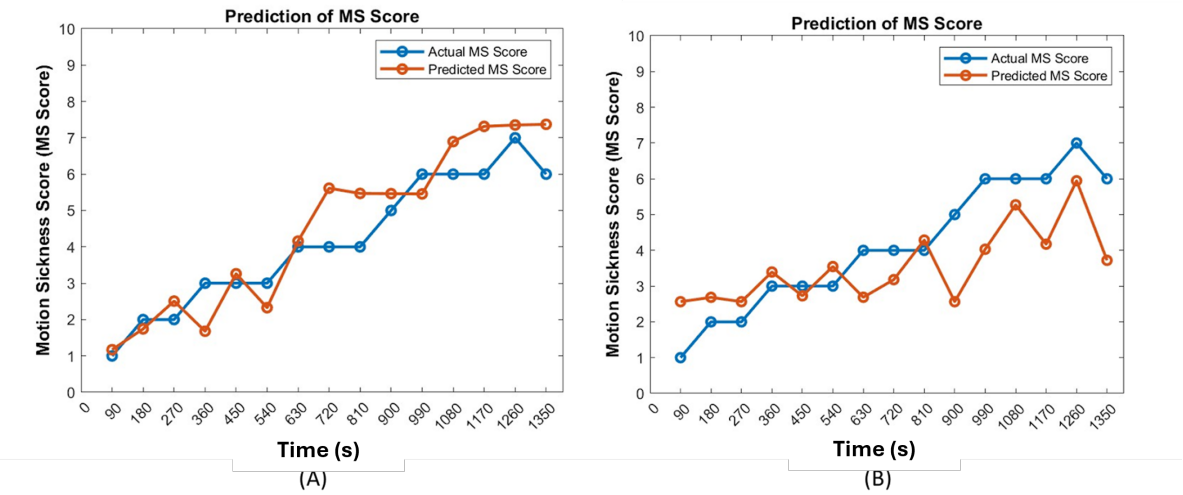


Figure 5.8: Predicted and true MS scores for (A) NARX (B) LSTM for a representative subject

model, SVM, with a time offset of 4 steps.

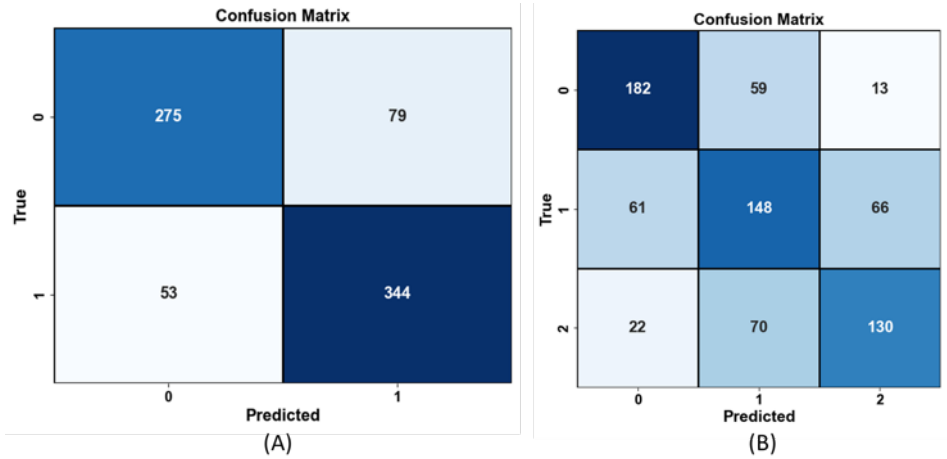


Figure 5.9: SVM confusion matrices using time-offset method (n=4) for (A) Binary and (B) Ternary Classification

5.4 Discussion

A comprehensive statistical analysis was conducted to determine the optimal predictive regression model by comparing the performance metrics of the NARX and LSTM approaches. The LSTM model resulted in a mean RMSE Error = 2.33. The results indicate that the

Table 5.12: Performance of binary classification models. The bold red text indicates the best performance instance for a given model.

Modeling	**SVM**			**Random Forest**			**XG Boost**		
Feature extraction	**F1**	**AUC**	**Accuracy**	**F1**	**AUC**	**Accuracy**	**F1**	**AUC**	**Accuracy**
Current Window	0.705	0.786	0.716	0.678	0.736	0.704	0.650	0.747	0.660
Expanding Window	0.773	0.870	0.790	0.723	0.800	0.738	0.740	0.810	0.756
Time-Offset, n = 1	0.783	0.857	0.786	0.714	0.795	0.719	0.738	0.804	0.744
Time-Offset, n = 2	0.775	0.848	0.793	0.763	0.835	0.771	0.770	0.845	0.779
Time-Offset, n = 3	0.814	0.868	0.816	0.727	0.807	0.731	0.774	0.838	0.779
Time-Offset, n = 4	**0.832**	**0.882**	**0.836**	**0.776**	0.846	**0.782**	0.774	**0.861**	0.777
Time-Offset, n = 5	0.780	0.831	0.786	0.747	0.826	0.754	0.774	0.853	**0.795**
Time-Offset, n = 6	0.794	0.875	0.797	0.754	0.827	0.760	**0.779**	0.848	0.782
Time-Offset, n = 7	0.748	0.845	0.753	0.722	0.812	0.730	0.756	0.838	0.759
Time-Offset, n = 8	0.766	0.854	0.768	0.742	**0.847**	0.748	0.746	0.819	0.752
Time-Offset, n = 9	0.784	0.841	0.787	0.752	0.822	0.757	0.741	0.839	0.756
Time-Offset, n = 10	0.761	0.821	0.763	0.752	0.841	0.757	0.761	0.844	0.766

Table 5.13: Model prediction results for binary and ternary classification approaches. The results presented correspond to the best-performing feature extraction methods for each model. All models yielded the best results using the time-offset method, with the number of steps ranging between 4 and 6.

Modeling	**SVM**			**Random Forest**			**XG Boost**		
Labeling	**F1**	**AUC**	**Accuracy**	**F1**	**AUC**	**Accuracy**	**F1**	**AUC**	**Accuracy**
Binary	0.832	0.882	0.836	0.776	0.846	0.782	0.779	0.848	0.782
Ternary	0.612	0.800	0.613	0.536	0.738	0.553	0.562	0.601	0.587

NARX model outperformed the LSTM, with lower mean RMSE values (Error = 2.097, dError = 0.671). This could be attributed to the short-term dependencies of MS scores on IMU data and the relatively small dataset available for training. A relevant aspect of this analysis is the interpretability of the results. The scale presented to subjects for collecting MS scores ranged from 0-10, and it was broken down into low, moderate, and high-intensity levels, with 3-4 points in the scale spanning each level. Hence, the regression model was able to predict the intensity of MS scores with higher resolution than the intensity categories presented to the subjects during the explanation of the MS score scale, yielding promising capabilities in predicting MS.

For binary MS classification, the SVM model exhibited the highest performance among the tested machine learning algorithms, achieving an accuracy of 83.66%. This result represents a marked improvement over the Random Forest and XGBoost classifiers, which achieved 78.23% and 78.2% accuracy, respectively. SVM's capacity to construct a decision boundary that generalizes effectively is advantageous when working with sparse or noisy data. The similar performance of XGBoost and Random Forest is likely due to their common decision tree-based architecture. It's important to note that for SVM to be effectively implemented for MS prediction, the feature set must be reduced to include only the most relevant features, since SVM performance can be substantially degraded with high-dimensionality datasets.

Moreover, the time-offset technique was identified as the most effective method for classification feature extraction. The optimal configurations for each model incorporated time-offset values of n=4, with each step consisting of 90 seconds. This indicates that a human's perception of MS intensity can lag the exposure to MS-eliciting head motion (resulting from vehicle accelerations) by up to 360 seconds. Considering this range of past windows achieves a balance by providing adequate information about preceding time windows while avoiding excessive dimensional expansion. The expanding window technique yielded lower accuracy than the top-performing time-offset configurations, indicating that the reduction in data

granularity negatively impacts model performance. Utilizing only the current time window resulted in an accuracy reduction of 10% or more relative to the optimal configuration for each model, underscoring the significance of processing historical data in MS prediction. This presents a significant insight for developing data-driven MS models, as the currently available models do not include time series feature engineering methods that leverage historical data.

The SVM model also achieved the highest performance for ternary classification, with an accuracy of 61.37%, a modest improvement over the 58.78% accuracy of the XGBoost algorithm and the 55.32% accuracy of the Random Forest algorithm. All three models encountered the most difficulty predicting the high MS class, as seen in the example shown in Figure 5.9. This can be attributed to the dataset having proportionally fewer data points in the high MS class. A dataset with more instances of high MS scores could improve model ternary classification performance.

5.5 Conclusion & Future Work

In this article, a machine learning framework was proposed to predict time series MS scores for passengers in a moving vehicle, using passenger head IMU data. A deep-learning regression model approach was initially presented, leveraging NARX and LSTM models. NARX showcased better results than LSTM and yielded promising results, with the RMSE statistic of 2.1. This RMSE value is smaller than the range of MS scores in each intensity category (low, medium, high) provided to the subjects when instructing them on the MS scale, as each category spans a MS score of approximately 3. This showcases the model's ability to accurately predict MS scores within the context of the scale used. Further, a binary and ternary classification approach was proposed, leveraging feature engineering methods and multiple classification algorithms, including SVM, Random Forest, and XG Boost. An investigation of classification performance indicated that the SVM model with a time-offset

engineering method yielded the best results, achieving 83.7% accuracy for binary classification and 61.37% for ternary classification. A time-offset range of 360 seconds was identified as the best-performing one, indicating that this is the most relevant range of historical IMU data for MS prediction. While the results are promising for MS prediction, the model can benefit from a larger dataset, as evidenced by the performance of the ternary classification algorithm in predicting samples in the high MS class. The proposed data-driven approach is fundamental in addressing one of the key deficiencies with MS prediction models, which often cannot account for individual and demographic variabilities in MS response. Furthermore, the diversity of the dataset used to train the models presented here provides confidence in the generalizability of the results presented, which is often a concern in the field of MS modeling. Finally, the classification framework proposed here is not only applicable to MS prediction but to any time series prediction modeling problem in which the output variable is highly dependent on historical input data.

This research allows accurate data-driven real-time prediction of MS scores using head motion data. The insights provided by this modeling framework can be used to design MS mitigation interventions, such as active systems that can modulate passenger head motion dynamics. In addition, this model can be further refined by including other relevant input data. For instance, the existing literature has established that cabin environmental parameters, such as temperature, humidity, air toxicity, ionization, and oxygen levels, influence human subjects' physiological state (i.e., MS intensity). An enhanced model incorporating a broader set of input variables and model parameters could be developed to ameliorate the predictive accuracy. Since MS affects various physiological parameters, developing models mapping each parameter could explore the impact of heart rate, skin perspiration, and surface electromyographic. The following chapter explores the use of physiological data for MS prediction purposes.

CHAPTER 6

Physiological Data-Driven Models for Motion Sickness Prediction

In-vehicle occupant monitoring systems are anticipated to play an instrumental role in the real-time evaluation of occupants' physiological states. Hence, the quantification of motion sickness (MS) intensity emerges as a critical component for in-vehicle applications. This requires analyzing physiological biomarkers to infer MS severity with high fidelity. The resultant estimations can be utilized as instantaneous feedback for the vehicle's control architecture or other vehicle systems, thereby facilitating adaptive modulation of its dynamic parameters. In alignment with this objective, this Chapter delineates the proposed classification-driven predictive models, accompanied by an assessment of the prioritization of data streams and corresponding features.

By leveraging a similar classification framework as the one proposed in Chapter 5, it's possible to implement data-driven models for MS prediction leveraging physiological data. This Chapter describes the additional processes required to adapt the data preprocessing and modeling implementation steps to achieve prediction capabilities with physiological data. These modifications are required due to the nature of physiological data, which require an ability to normalize the data across multiple individuals and the ability to reconcile different sensor information. The use of this type of data has the potential to enable real-world deployment of these prediction algorithms by using in-cabin physiological monitoring sensors.

6.1 Data Preprocessing

Figure 6.1 shows the flowchart for preprocessing the data and generating the relevant physiological features for model training. The collected Electrodermal Activity (EDA), Blood Volume Pulse (BVP) and Surface Electromyography (sEMG) physiological data were temporally aligned with the onset of the MS score recording via Universal Coordinated Time (UTC) timestamps to ensure precise temporal correspondence. Data segmentation was terminated upon the fulfillment of any one of the following three criteria: completion of three full laps around the test track, attainment of a maximum MS score of 10 by the participant, or the occurrence of a sensor malfunction. The Blood Volume Pulse (BVP) signal was subjected to an 8 Hz low-pass filter to accentuate the spectral components most pertinent to MS modeling [88]. A convex optimization method [89] was used to separate the Electrodermal Activity (EDA) data into into tonic (< 0.05 Hz) and phasic (> 0.05 Hz) components to facilitate finer-grained signal analysis. This method enables the separation of the EDA signal into tonic, phasic and noise data segments, further improving the data quality. The E4 sensor did not directly record heart rate; instead, it was derived as the reciprocal of the mean interbeat interval, yielding an estimated heart rate parameter.

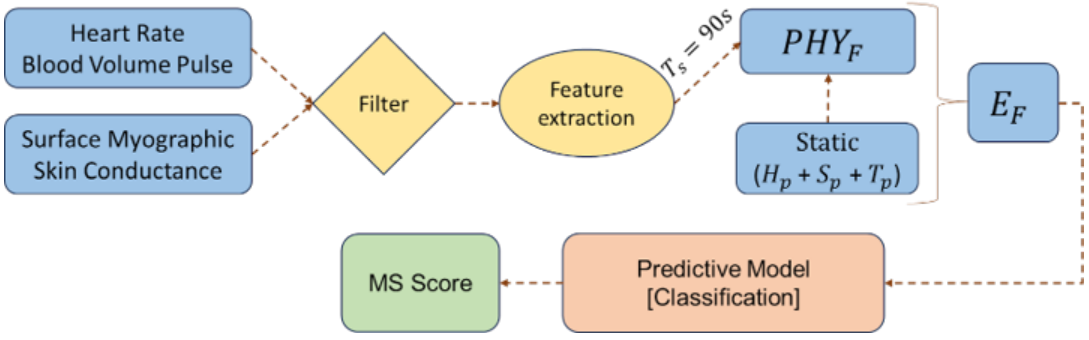


Figure 6.1: Physiological Modeling Data Preprocessing Flowchart

Surface electromyography (sEMG) data acquisition generated two signal streams from the left and right sternocleidomastoid (SCD) muscles. The two SCD streams were aggregated by summation to yield a composite signal representing overall sEMG amplitude. This allowed

for dimensionality reduction while preserving the data streams from both sensors. Due to the high susceptibility of sEMG signals to environmental artifacts, such as motion-induced distortion, baseline drift, and power-line interference, several preprocessing steps were employed to enhance signal integrity. Specifically, a second-order Butterworth bandpass filter with a passband of 20–500 Hz, alongside a 50 Hz notch filter, was applied to attenuate noise and eliminate extraneous frequency components [90].

Similar to the model proposed in Chapter 5 Table 5.1, a static vector was conjugated with three components $[H_P]$, $[T_P]$, and $[S_P]$, as defined in Table 6.1. The demographics were integrated with $[H_P]$, whereas the experimental conditions, which include the task type and state of HSS, were defined with $[T_P]$ and $[S_P]$. Ultimately, the input vector for the predictive model $[E_F]$ was constructed by integrating the dynamic features of the physiological data, shown in Table 6.2, with the static vector components as shown in Figure 6.1. In total, 17 participants completed all three test conditions, 8 participants completed two test conditions and 4 participant completed only one test condition.

6.2 Predictive Modeling

To render the processed physiological data suitable for predictive modeling, a range of feature engineering techniques was employed. Each physiological signal was segmented into 90-second windows, aligned with the sampling frequency of the corresponding MS score. For each trial, a single 90-second segment of data collected 2–3 minutes before trial onset was designated to characterize the subject's baseline physiological state. Feature extraction was conducted by calculating quantitative descriptors from physiological data. The extracted features encompassed time-domain features for all data streams, and frequency-domain features specifically for blood volume pulse (BVP) and surface electromyography (sEMG) signals as described in Table 6.2. Furthermore, static demographic and experimental condition variables, such as age, gender, and trial context, were incorporated. Detailed feature names and

Table 6.1: Static features considered for model prediction

Static Variables	**Magnitudes**		
H_P	[gender, susceptibility, age]		
S_P	[HSS active, HSS inactive]		
T_P	[task, no task]		
Age distribution	Females: [18 32]; Males: [19 34]		
Gender distribution	16 Female, 13 Male		
Trial distribution	38 Female, 33 Male		
Susceptibility index	Low [1]; Medium [2]; High [3]		
Gender (M/F)	Male (2)	Female (1)	
Test conditions (TC)	(TC1) [HSS active, No Task]	(TC2) [HSS inactive, Task]	(TC3) [HSS active, Task]

descriptions are provided in Table 6.2 and were obtained based on an list of prior studies collected under the NeuroKit python library [91, 92]. An exhaustive list of these features was used due to the ability to reduce dataset dimensionality at later stages by leveraging feature selection methods.

Table 6.2: Definition of Phyisiological data dynamic features

Property	**Description**
Frequency Domain	
Power Spectral Density	$PSD_{xx}(f_k) = \frac{1}{N} \lvert X(f_k) \rvert^2$ where $X(f_k)$ is the Discrete Fourier Transform of signal $x[n]$ with length N evaluated at frequency f_k.
BVP Low Frequencies	$LF = \int_{0.04}^{0.15} PSD(f)df$ where $P(f)$ is the power spectral density of the BVP signal at frequency f.
BVP High Frequencies	$HF = \int_{0.15}^{0.4} PSD(f)df$
BVP Very High Frequencies	$VHF = \int_{0.4}^{0.5} PSD(f)df$

BVP Total Power	$TP = \int_0^N PSD(f)df$ where N is the nyquist frequency (32 Hz in this work).
BVP Low Frequency-High Frequency	$LFHF = \frac{LF}{HF}$
BVP Low Frequency normalized	$LFn = \frac{LF}{TP}$
BVP High Frequency normalized	$HFn = \frac{HF}{TP}$
BVP Log-Transformed High Frequencies	$LnHF = \ln(HF)$
EDA Sympathetic	$EDA_{\text{sympathetic}} = \int_{0.045}^{0.25} PSD(f)df$ where $P(f)$ is the power spectral density of the EDA signal at frequency f.

EDA Sympathetic N	$$EDA_{\text{sympathetic N}} = \frac{EDA_{\text{sympathetic}}}{\int_0^N PSD(f)df}$$ where N is the nyquist frequency (2 Hz in this work).
sEMG Mean Frequency	$$MNF = \frac{\sum_{l=1}^{M} f_l p_l}{\sum_{l=1}^{M} p_l}$$ Where f_l is the spectral frequency in the bin of frequency l, p_l is the EMG signal power spectrum in the bin l, and M is the frequency bin length.
sEMG Median Frequency	$$\sum_{l=1}^{MDF} P_l = \sum_{l=MDF}^{M} P_l$$ It is the frequency divided into two regions with the same amplitude; that is to say, MDF is the total power average and could be expressed as the number MDF with the property where P_l is the EMG signal power spectrum at a frequency bin l, and M is the frequency bin length.
sEMG Peak Frequency	$$PKF = (p_l)$$

sEMG Mean Power	$$MNP = \frac{\sum_{l=1}^{M} p_l}{M}$$
sEMG Total Power	$$TTP = \sum_{l=1}^{M} P_l$$
sEMG Frequency Ratio	$$FR = \frac{\sum_{l=LLC}^{ULC} p_l}{\sum_{l=LHC}^{UHC} p_l},$$ Where ULC and LLC are upper and lower coefficients of the cutoff frequency of the low band frequency and UHC and LHC are those from the high frequency, respectively.
sEMG Power Spectrum Ratio	$$PSR = \frac{P_0}{P}$$ where $$P_0 = \sum_{l=f_0-n}^{f_0+n} P_l \quad \text{and} \quad P = \sum_{l=-\infty}^{\infty} P_l$$ with f_0 the PKF value and n a hyperparameter.
sEMG Power Spectral Density	$$PSD(f) = \lvert X(f) \rvert^2$$ where X is the Discrete Fourier Transform.

sEMG Frequency Mean Density	$FMN(f) = \frac{\sum_{i=1}^{M} f_i PSD_i}{\sum_{i=1}^{M} PSD_i}$
sEMG Frequency Median Density	$FMD(f) = \frac{1}{2}\sum_{i=1}^{M} PSD_i$
sEMG First, Second and Third Spectral Movements	$SM_i = \sum_{l=1}^{M} P_l f_l^i$
sEMG Variance of Central Frequency	$VOC = \frac{1}{TTP}\sum_{l=1}^{M} P_l(f_l - f_c)^2$
Time Domain	
BVP NN Interval	R = The array of times between consecutive peaks (R-R intervals) in a BVP signal with artifacts removed.
BVP Mean NN	$MeanNN = \frac{\sum_{n=0}^{N} R_n}{N}$ where R_n is the NN-interval at index n and N is the number of intervals.

BVP Standard Deviation NN	$$SDNN = \sqrt{\frac{1}{N-1}\sum_{i=1}^{N}(R_i - \bar{R})^2}$$ where R_i is the NN-interval at index i and N is the number of intervals.
BVP SDANN1, SDANN2, SDANN5	$$SDANN_k = \sqrt{\frac{1}{N-1}\sum_{i=1}^{N}(R_{k,i} - \overline{R_k})^2}$$ where R_k is the set of mean NN intervals over segments of length k. Here we use $k = 1, 2, 5$.
BVP SDNNI1, SDNNI2, SDNNI5	$$SDNNI_k = \frac{\sum_{i=0}^{N} R_{k,i}}{N}$$ where R_k is the set of NN interval standard deviations over segments of length k. Here we use $k = 1, 2, 5$.
BVP RMSSD	$$RMSSD = \sqrt{\frac{1}{N-1}\sum_{i=1}^{N-1}(R_{i+1} - R_i)^2}$$

BVP SDSD	$$SDSD = \sqrt{\frac{1}{N-2}\sum_{i=1}^{N-1}\left(d_i - \bar{d}\right)^2}$$ where $$d_i = R_{i+1} - R_i \quad \text{for } i = 1, 2, \ldots, N-1$$
BVP CVNN	$$CVNN = \frac{SDNN}{MeanNN}$$
BVP CVSD	$$CVSD = \frac{RMSSD}{MeanNN}$$
BVP MedianNN	$$MedianNN = \text{median}(R_1, R_2, \ldots, R_n)$$
BVP MadNN	$$MadNN = \mid R_n - MedianNN \mid \quad \text{for } i = 1, 2, \ldots, N$$
BVP MCVNN	$$MCVNN = \frac{MadNN}{MedianNN}$$
BVP IQRNN	The interquartile range of the NN-intervals.

BVP SDRMSSD	$SDRMSSD = \frac{SDNN}{RMSSD}$
BVP Prc20NN	The 20th percentile of the NN-intervals.
BVP Prc80NN	The 80th percentile of the NN-intervals.
BVP pNN50	$pNN50 = \frac{N_{50}}{N}$ where N_{50} is the number of NN-intervals that exceed 50 milliseconds.
BVP pNN20	$pNN20 = \frac{N_{20}}{N}$ where N_{20} is the number of NN-intervals that exceed 20 milliseconds.
BVP MinNN	$NN_{\min} = \min_{n} R$
BVP MaxNN	$NN_{\max} = \max_{n} R$

BVP TINN	Let H be a histogram of NN-intervals and t be the triangle function that plots a point N_2 at the mode and points N_0, N_1 at both ends of H such that the difference between the area of t and the area of H is minimized. $$TINN = N_1 - N_0$$
BVP HTI	$$HTI = \frac{N}{\max_n H[n]}$$ where N is the total number of NN-intervals and H is the histogram of NN-intervals.
HR Standard Deviation	$$HR_\sigma = \sqrt{\frac{1}{N-1}\sum_{i=1}^{N}(x_i - \bar{x})^2}$$ where x_i is the heart rate at sample index i and $\overline{x}$ is the average heart rate over the given time window.
HR Maximum	$$HR_{\max} = \max_n x[n]$$ where $x[n]$ is the heart rate signal.
HR Minimum	$$HR_{\min} = \min_n x[n]$$

EDA SCR Peaks N	The number of peaks in the phasic component. A peak is defined as $SCR_{peaks}(s) = \{n \in [1, N] \mid s[n] > 0.1 \cdot A_{max}\}$ where s is the phasic component and A_{max} is the maximum amplitude of the signal from $t = [0, N]$.
EDA SCR Peaks Amplitude Mean	The mean amplitude of the skin conductance response peak occurrences.
EDA Phasic	$s_{\text{phasic}}(t) = \mathcal{H}_{\text{HP},0.05}\{s(t)\}$ where $s(t)$ is the EDA signal, and $\mathcal{H}_{\text{HP},0.05}$ is a high-pass filter applied with cutoff frequency 0.05 Hz.
EDA Tonic	$s_{\text{tonic}}(t) = \mathcal{H}_{\text{LP},0.05}\{s(t)\}$ where $\mathcal{H}_{\text{LP},0.05}$ is a low-pass filter applied with cutoff frequency 0.05 Hz.
EDA Tonic Standard Deviation	The standard deviation of the tonic component, $s_{\text{tonic}}(t)$.
EDA Autocorrelation	$EDA_{\text{autocorrelation},xx}[k] = \sum_{n=0}^{N-k-1} x[n] \cdot x[n+k]$ where k is the lag (4 seconds in this work) and N is the maximum window size (90 seconds in this work).

sEMG Average Amplitude Value	$AAV = \frac{1}{N}\sum_{k=1}^{N} x_k$
sEMG Mean Absolute Value	$MAV = \frac{1}{N}\sum_{k=1}^{N} \lvert x_k \rvert$
sEMG Modified Mean Absolute Value	$MMAV = \frac{1}{N}\sum_{k=1}^{N} w_k \lvert x_k \rvert$ where $f(x) = x$ if $x > 0$ else 0.
sEMG Variance	$VAR = \frac{1}{N-1}\sum_{k=1}^{N} x_k^2$
sEMG Zero Crossings	ZC is the count of the zero crossings for the signal.
sEMG Average Amplitude Change	$AAC = \frac{1}{N}\sum_{k=1}^{N} \lvert x_{k+1} - x_k \rvert$
sEMG Simple Square Integral	$SSI = \sum_{k=1}^{N} x_k^2$

sEMG Slope Sign Changes	$$SSC = \sum_{i}^{n} f_{ssc}(x_i),$$ $$f_{ssc} = \begin{cases} 1, & \text{if } x_i < x_{i+1} \text{ and } x_i < x_{i-1} \\ 1, & \text{or } x_i > x_{i+1} \text{ and } x_i > x_{i-1} \\ 0, & \text{otherwise} \end{cases}$$ This feature allows another description of the frequency; it is the number of times that a slope sign changes occur.
sEMG Waveform Length	$$WL = \sum_{k=1}^{N} \lvert x_k - x_{k-1} \rvert$$ WL is the accumulated waveform length above the time segment.
sEMG Wilson Amplitude	$$WAMP = \sum_{k=1}^{N-1} f(\lvert x_{k+1} - x_k \rvert)$$
sEMG Difference of Absolute Standard Deviation	$$DASDV = \sqrt{\frac{1}{N-1} \sum_{k=1}^{N-1} (x_{k+1} - x_k)^2}$$

sEMG Absolute Value of Thid, Fourth and Fifth Temporal Moments (TM3, TM4, and TM5)	$TM_i = \lvert\frac{1}{N}\sum_{k=1}^{N} x_k^i\rvert$
sEMG Myopulse Percentage Rate	$MYOP = \frac{1}{N}\sum_{k=1}^{N} \phi(x_k)$
Number of high bins	$\mu_k^{(5)} = \frac{1}{5}\sum_{j=0}^{4} x_{k+j}, \quad \text{for } k = 1, 2, \ldots, N-4.$ $\text{num_high_bins} = \sum_{k=1}^{N-4} \psi\left(\mu_k^{(5)} > 2\mu\right),$

The use of human subjects in variable environmental conditions introduces considerable heterogeneity into the data, which may degrade model performance. To mitigate this issue, three normalization strategies were devised and assessed, and their descriptions are provided in the paragraph below. When applied, normalization was conducted on a per-feature basis, relative to the subject's baseline value for the corresponding trial. The feature normalization method used the following relationship:

$$Normalized_Feature = \frac{(Raw_Feature - Baseline_Feature)}{Baseline_Feature} \tag{6.1}$$

In addition to the choice of normalizing the features, another choice involved including or excluding baseline windows in the set of predictive features within the dataset. Including the baseline window as part of the predictive feature set increases sample size but disproportionately augments the number of samples labeled with an MS score of zero. The three

normalization strategies were conducted as follows:

- Method A: No normalization was applied, and the baseline window was excluded.
- Method B: All features were normalized to their corresponding baseline values; however, the baseline window was omitted from the predictive feature set.
- Method C: All features were baseline-normalized, and the baseline window was included in the dataset. Details of the feature importance evaluation are presented in the following sections.

One limitation of using the Empatica E4 wristband is that the BVP signals are susceptible to noise and motion artifacts since the sensor leverages photoplethysmography for measurement. Gao et al. [93] previously identified these limitations and proposed a signal quality analysis (SQA) model to predict the reliability of BVP signal segments. This SQA model is able to detect issues with BVP data based on wrist motion artifacts, which lead to noise in the photoplethysmography sensor of the E4 wristband. Leveraging their pretrained model, an SQA model was deployed to assess the quality of the BVP signal within dataset. The BVP signal was divided into 10-second epochs, each labeled as high or low quality based on the model's output. SQA analysis indicated that only 43% of the BVP data was considered high-quality data, underscoring a fundamental limitation with the sensor used. While this SQA method has been shown to predict 85% of bad quality data points correctly, it doesn't provide a framework for handling bad-quality data for data analysis purposes.

With this in mind, three signal augmentation techniques were developed and evaluated to address low-quality epochs. The forward fill method replaced the low-quality epoch with data from the most recent preceding high-quality epoch. The interpolation method substituted the epoch with a linear interpolation between the nearest preceding and succeeding high-quality epochs. The baseline padding method replaced the epoch with the average BVP signal computed from the baseline window of the corresponding trial.

The classification models employed in this study require input data of fixed dimensionality. As a result, feature vectors of varying lengths cannot be processed by the same model configuration, thereby constraining the model's capacity to incorporate temporal dependencies from earlier data when making predictions. To address this constraint, while preserving the temporal dynamics of motion sickness (MS) across the duration of each trial, the two feature extraction strategies proposed in Chapter 5 were implemented.

The first approach, the expanding window technique, generated two feature vectors per time point: one representing the most recent 90-second data segment, and another summarizing all preceding 90-second windows. The historical vector was computed by averaging feature values from the start of the trial until the current window. The diagram for this process is shown in Figure 5.5. The second strategy, the time-offset method, was designed to handle variable-length feature vectors without aggregation. Rather than summarizing earlier segments, this method retains the previous 90-second feature vectors as discrete entries. For more details on these approaches, refer to Chapter 5 Section 5.2.2.

The time-offset approach shown in Chapter 5 Figure 5.6 constructs the feature matrix by vertically stacking feature vectors from each 90-second window such that rows correspond to time windows and columns to individual features. To introduce temporal lag, the matrix is duplicated and shifted downward by one row to form lagged features. This operation is repeated for the desired number of time offsets, and the resulting matrices are concatenated horizontally in chronological sequence. Inevitably, the shifting process leads to missing entries corresponding to the earliest time steps. To maintain consistent input dimensions, these entries were filled using baseline feature vectors derived from the initial phase of the trial. The final compiled feature matrix for each trial is obtained by vertically stacking all individual trial matrices, ensuring that the feature representation for any given time window includes data from preceding intervals. This approach aligns with the cumulative nature of MS, wherein past conditions significantly influence the current state, thus enhancing the model's ability to learn temporal dependencies. The impact of varying the number of time-

offset windows on model performance is addressed in the Section 6.2.

This study investigated both binary and ternary classification schemes. For binary classification, MS scores from 0 to 2 were labeled as low, while scores from 3 to 10 were labeled as high. For ternary classification, scores of 0–1 were labeled as low, 2–4 as medium, and 5–10 as high. These thresholds were designed to balance the class distribution and to reflect meaningful ranges in MS intensity as experienced by passengers.

To prevent data leakage and preserve model integrity, the dataset was partitioned at the trial level, ensuring that all samples from a given trial were assigned exclusively to either the training or testing set. From the complete set of 71 trials considered in this study, 80% were allocated for training and 20% for testing. Model hyperparameters were optimized using grid search with 5-fold cross-validation. For details regarding the K-fold method used, refer to Chapter 5 Section 5.2.2 Figure 5.7.

For the Support Vector Machine (SVM), hyperparameter tuning focused on optimizing the gamma parameter, which controls the decision boundary smoothness, and the regularization parameter C. For the Random Forest model, the maximum tree depth and number of trees were optimized. Feature selection was conducted using K-fold cross-validation, where Gini importance was calculated over 100 iterations of the Random Forest to estimate the relative contribution of each feature. While Random Forest models achieved optimal performance with the full feature set, the SVM, being more susceptible to overfitting in high-dimensional settings, required dimensionality reduction. The five most important features, as identified by Gini importance, were selected for the SVM. Furthermore, an grid search identified the optimal combination of three frequency-domain and three time-domain features. These six features were combined with the top five to produce a final SVM feature set comprising 11 features. The use of the top 5 features was done to ensure the top features with highest order of magnitude in terms of Gini importance were included in the dataset. The use of three time-domain and frequency-domain features was employed to ensure representation of both feature domains in the dataset. The decision to limit the number of

features to 11 was made based on an evaluation of the maximum dimensionality suitable for SVM modeling without compromising model performance.

6.3 Results

The preprocessed physiological data was input for training machine learning models to classify motion sickness (MS) levels at 90s discrete time points. Model performance was evaluated using accuracy, F1-score, and the area under the receiver operating characteristic curve (AUROC), with accuracy designated as the principal metric for comparative analysis. Evaluation was conducted using binary and ternary classification schemes, as presented in Table 6.3. The confusion matrices for binary and ternary classification are shown in Figures 6.2 and 6.3, respectively.

Table 6.3: Binary and ternary classification model performance

Labels	**Model**	**Accuracy**	**AUROC**	**F1 Score**
Binary	SVM	0.7810	0.7748	0.8819
Ternary	SVM	0.5483	0.5443	0.7478
Binary	RF	0.8141	0.8110	0.8846
Ternary	RF	0.5828	0.5912	0.7522

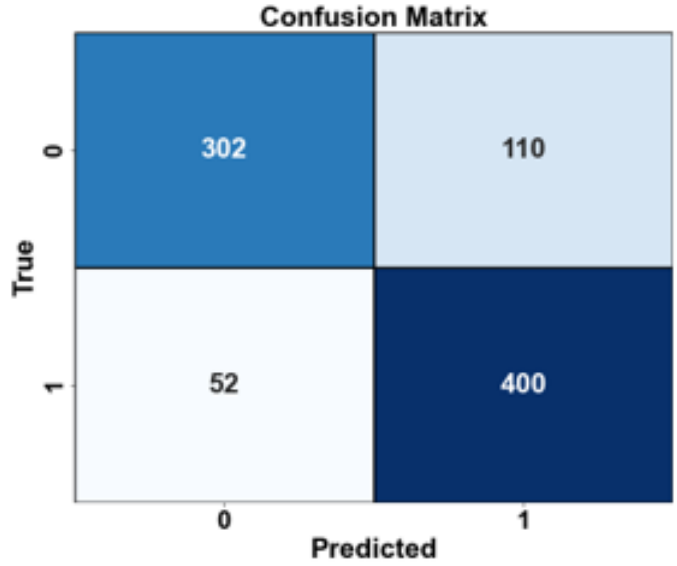


Figure 6.2: Sample Random Forrest confusion matrix for binary classification

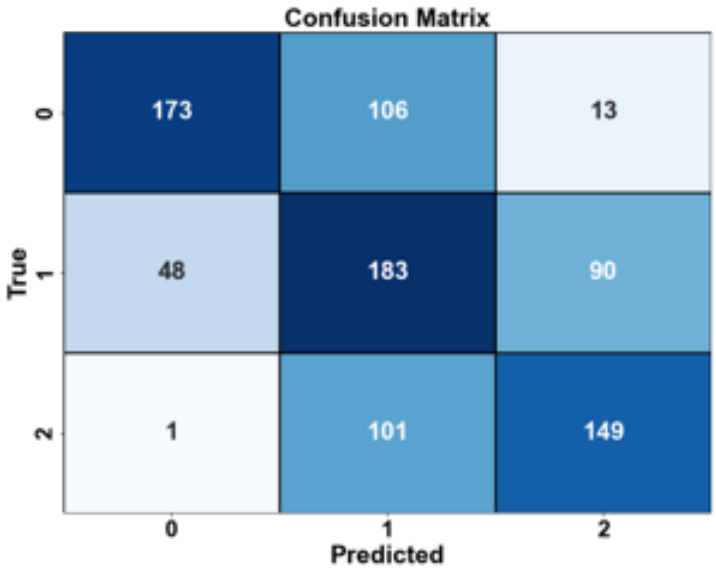


Figure 6.3: Sample Random Forrest confusion matrix for ternary classification

Furthermore, the impact of various normalization techniques on model performance is summarized in Table 6.4. Table 6.5 illustrates the performance outcomes of different blood volume pulse (BVP) signal augmentation strategies employing signal quality assessment

(SQA). Figure 6.4 depicts the influence of varying feature extraction time offset windows on classification performance.

Table 6.4: Classification Model performance for different data normalization techniques.

Normalization Method	**Accuracy**	**F1-Score**	**AUROC**
A	0.7338	0.7157	0.8154
B	0.7630	0.7560	0.8644
C	0.8141	0.8110	0.8846

Table 6.5: Classification Model performance for different BVP data augmentation techniques.

Augmentation	**Accuracy**	**AUROC**	**F1 Score**
None	0.739	0.76	0.745
Padding	0.7876	0.7807	0.7644
Interpolation	0.7968	0.805	0.7665
Forward Fill	0.7922	0.776	0.8024

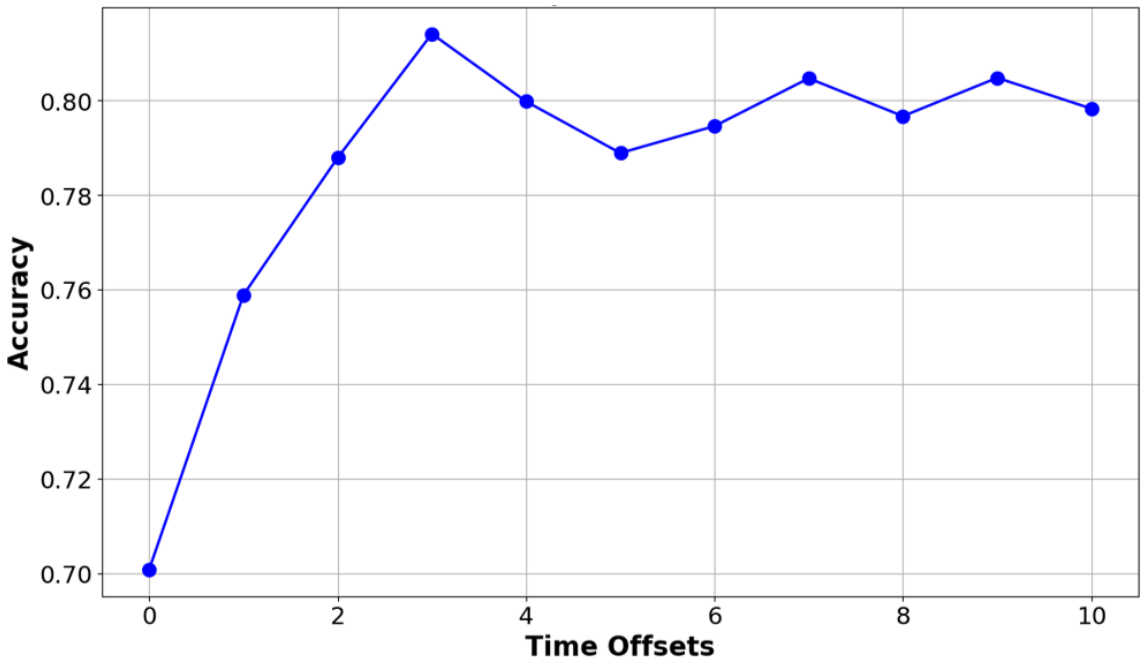


Figure 6.4: Classification accuracy model performance for different time offsets.

Gini-based feature importance was used to identify the most informative predictors for MS classification, assessed across features and time windows. This was also performed to analyze the importance of the time-offset windows for physiological data, as shown in Table 6.6. This Table reports the relative importance of each time window aggregated across all features. The overall contribution of each physiological data was also analyzed and shown in Table 6.7. The top 10 most important features across all data streams are displayed in Table 6.7. The complete list of features and their calculated importance is shown in Table 6.8. All feature importance metrics were multiplied by 100 for easier comprehension. For each table, the Random Forest parameters that maximized accuracy were used.

Table 6.6: Gini importance for different physiological time-offset windows.

Time Offset	**Importance (x100)**
0	30.84
1	16.47
2	7.95
5	7.06
4	6.88
3	6.57
10	5.97
7	5.92
8	5.82
6	5.78
9	5.69

Table 6.7: Gini importance for different physiological data streams.

Data Stream	**Average Importance (x100)**	**Maximum**	**Minimum**
Electrodermal Activity	2.289	Tonic SD = 3.122	Autocorrelation = 1.162
sEMG	1.620	Max Value = 4.721	Mean Difference Value = 0.741
Blood Volume Pulse	0.924	pNN50 = 1.378	MinNN = 0.688
Heart Rate	0.921	Max Value = 1.028	Min Value = 0.713

Table 6.8: Gini importance for different physiological features.

Feature	**Importance (x100)**
sEMG_MaxValue	4.721
Phy_EDA_Tonic_SD	3.122
Phy_SCR_Peaks_N	2.88
Phy_SCR_Peaks_Amplitude_Mean	2.866
Phy_EDA_Sympathetic	2.37
sEMG_AbsoluteValueOfTheFifthTemporalMoments	2.319
sEMG_AbsoluteValueOfTheFourthTemporalMoments	2.212
sEMG_AbsoluteValueOfTheThirdTemporalMoments	2.2
sEMG_StandardDeviation	2.181
sEMG_WillsonAmplitude	2.168
sEMG_DifferenceOfAbsoluteStandardDeviation	2.115
sEMG_MyopulsePercentageRate	1.936
sEMG_WaveformLength	1.716
sEMG_AverageAmplitudeChange	1.695
sEMG_MeanPower	1.654

sEMG_TotalPower	1.596
sEMG_numberOfSmallBins	1.543
sEMG_The2ndSpectralMovements	1.49
sEMG_FrequencyRatio	1.487
sEMG_VarianceOfCentralFrequency	1.456
sEMG_ModifiedMeanAbsoluteValueType1	1.451
sEMG_The1stSpectralMovements	1.441
sEMG_PeakFrequency	1.425
sEMG_The3rdSpectralMovements	1.413
sEMG_SlopeSignChanges	1.405
sEMG_MeanFrequency	1.4
Phy_BVP_pNN50	1.378
Phy_EDA_SympatheticN	1.338
sEMG_ModifiedMeanAbsoluteValueType2	1.335
sEMG_RootMeanSquareValue	1.206
Phy_BVP_CVSD	1.166
Phy_EDA_Autocorrelation	1.162
Phy_BVP_CVNN	1.045
Phy_BVP_HTI	1.045
Phy_BVP_TINN	1.037
Phy_BVP_HF	1.031
Phy_BVP_RMSSD	1.030
Phy_HR_Max	1.028
Phy_HR_SD	1.022
Phy_BVP_SDNN	1.000
Phy_BVP_SDSD	0.977
Phy_BVP_HFn	0.963

Phy_BVP_SDRMSSD	0.932
Phy_BVP_IQRNN	0.927
Phy_BVP_LF	0.909
Phy_BVP_Prc20NN	0.904
Phy_BVP_MaxNN	0.886
Phy_BVP_MCVNN	0.883
Phy_BVP_Prc80NN	0.865
sEMG_numberOfSuperLargeBins2	0.855
sEMG_MeanAbsoluteValue	0.827
Phy_BVP_LFn	0.792
sEMG_AverageAmplitudeValue	0.788
Phy_BVP_MeanNN	0.784
Phy_BVP_LFHF	0.780
Phy_BVP_MadNN	0.764
Phy_BVP_LnHF	0.747
Phy_BVP_MedianNN	0.745

Table 6.9 shows the effect of removing specific static features in terms of model predictive performance. With all static features included, the model is able to achieve 81% binary classification accuracy. The features that yielded the highest reduction in accuracy are the subject identifier (7.76%) and MS susceptibility (7.39%). The subject identifier allows the model to learn MS response patterns on an individual level, which has been shown to improve model performance significantly as shown in Table 6.9. The MS susceptibility is a measure of a subject's propensity to become motion sick based on a questionnaire answered ahead of the trial, and it is a good predictor of the intensity of MS.

Table 6.9: Effect of removal of static features in model prediction accuracy.

Feature Removed	**Accuracy Performance Decrease (%)**
Subject ID	7.76
MS Susceptibility	7.39
Gender	5.34
Age	4.40
Cognitive Task Indicator	1.84
Haptic Seat System Indicator	1.19

6.4 Discussion

This study evaluated established classification algorithms, such as SVM and Random Forrest, to identify the most effective approach for modeling motion sickness (MS) using physiological parameters. In binary classification tasks, the Random Forest and Support Vector Machine (SVM) models achieved accuracies of 81.41% and 78.10%, respectively as seen in Table 6.3. For ternary classification, Random Forest achieved 58.28% accuracy and SVM achieved 54.83%. Both models exhibited the greatest difficulty in accurately predicting instances of the high MS class as observed in Figures 6.2 and 6.3. This limitation is primarily attributable to the dataset's class imbalance, with comparatively fewer samples corresponding to high MS severity. Enhancing the dataset with a greater number of high MS instances could improve

the models' ability to perform ternary classification more effectively.

The application of data normalization techniques resulted performance improvements as seen in Table 6.4. Specifically, incorporating each participant's baseline physiological data and normalizing trial data relative to that baseline led to the most favorable outcomes among the normalization strategies examined, yielding a 7.09% increase in accuracy compared to models trained on unnormalized data. On the other hand, normalizing the trial data but excluding the baseline window only led to a 3% improvement with respect to the benchmark. This suggests that the inclusion of the baseline window in the dataset results in improved performance when normalization methods are applied. This can be attributed to the additional windows available for training, as well as the additional information regarding how specific trial data is expected to behave based on the baseline physiological response. These results highlight substantial inter-individual variability in physiological responses and underscore the importance of normalization in enabling accurate modeling of MS.

Table 6.7 shows that, among the four streams of physiological data analyzed, electrodermal activity (EDA) emerged as the most informative for the prediction of MS, while heart rate (HR) contributed the least, which aligns with previous findings in the modeling of physiological signals. The blood volume pulse (BVP) signal exhibited instances of low data quality due to motion artifacts; however, applying signal quality assessment (SQA) to identify low-quality segments and subsequently augmenting these segments substantially mitigated the impact of noise as shown in Table 6.5. Interpolation of low-quality BVP data proved to be the most effective augmentation technique as shown in Table 6.5, improving prediction accuracy by 5.78% relative to models trained without data correction. These findings suggest that signal quality evaluation and augmentation algorithms are critical for ensuring robust BVP-based modeling, particularly when using photoplethysmography-based wearable devices such as the E4 wristband. Table 6.8 shows that electrodermal activity features comprise 4 out of the top 5 most important features for MS prediction. However, sEMG also showcased strong predictor importance, with one feature occupying the spot of

the most important feature. Further, sEMG features represented 6 out of the top 10 most important features. The highest placed BVP feature was ranked 27th in terms of feature importance.

The static features' effects on model performance were evaluated by quantifying the percentage decrease in accuracy when each of the features is removed. It was observed that the subject identifier and the subject's MS susceptibility showed the highest contribution towards model performance, yielding 7-8% improvement each. Other factors such as gender, age, and test condition were also shown to be relevant for MS prediction as shown in Table 6.9. These results underscore the importance of utilizing subject demographics and test conditions when predicting MS. The framework for the use of these features for MS prediction is a new development proposed by this work and expand on the capabilities of existing physiological and data-driven models.

The time-offset feature extraction method yielded an 11% improvement in accuracy for the Random Forest model when compared to the current window (zero time offsets) benchmark as seen in Figure 6.4. The Figure also shows that using up to 270s of time offset can lead to model improvements. On the other hand, feature importance analysis using Gini index revealed that data from the most recent 180 seconds provided the strongest predictive power as shown in Table 6.6. This can be attributed to the tradeoff that exists between feature importance and dataset dimensionality. While using more time offsets can provide more information for model predictions, it can also lead to higher dimensionality. If the importance of features do not outweigh the downsides of increasing dimensionality, the model will perform worse as more time offsets are included in the feature matrix.

The superior predictive value of relatively recent data, in contrast to the extended temporal relevance observed for head acceleration in Chapter 5, suggests that physiological responses serve as downstream indicators of MS onset, rather than precursors. Head motion exposure precedes a subject's self-reporting of MS by up to 360 seconds, while physiological data precedes it only by 180 seconds. Two possible conclusions can be drawn from this: (i)

the actual onset of MS occurs 360 to 180 seconds before subjects can notice symptom effects and physiological indicators lag the onset of MS, or (ii) subjects can only notice symptom effects 180 seconds after physiological response. In either case, these findings provide valuable insight into the temporal dependency of MS eliciting motion events, the physiological response of humans to MS, and human self-reporting of MS intensity.

6.5 Conclusion & Future Work

This study presents a framework for estimating individual motion sickness (MS) scores by leveraging novel time offset feature engineering methods, a suite of physiological signals (HR, BVP, EDA and sEMG), and a static demographic feature vector. Multiple predictive models were developed using established machine learning classifiers, including Support Vector Machines (SVM) and Random Forests. Among these, the Random Forest classifier achieved superior performance in the binary classification task, attaining a peak accuracy of 81.41%. The best ternary classifier, Random Forrest, achieved an accuracy of 58.28%. The limited sample size, particularly for instances of high MS severity, likely imposed constraints on model generalizability for the high MS intensity class. Crucially, normalization of baseline physiological features emerged as a pivotal preprocessing step to mitigate inter-subject variability and enhance model fidelity. The findings underscore the importance of EDA and sEMG signals as robust predictors of MS and further reveal that the temporal window spanning 0 to 180 prior to subjects' self-reporting of MS constitutes the most informative segment for prediction. While additional signal modalities demonstrated supplementary predictive utility, their effectiveness may be contingent upon further signal enhancement procedures, such as the application of Signal Quality Assessment (SQA) algorithms to rectify artifacts in BVP recordings.

Subsequent work will pursue a data-driven, iterative optimization process to expand the range of models considered and to achieve better training with a larger sample size. Future

investigations will investigate environmental parameters intrinsic to the vehicular cabin, such as cabin air temperature, relative humidity, and atmospheric composition, to modulate physiological state during transit. In its envisioned application, this modeling framework may be embedded within an adaptive, closed-loop system capable of delivering real-time physiological feedback to the vehicle's control unit or in-cabin systems, thereby facilitating dynamic adjustments to vehicular motion states in order to optimize passenger comfort.

CHAPTER 7

Conclusion and Future Work

The work presented in this thesis encapsulates different modeling frameworks to predict passenger motion sickness (MS) for on-road vehicles. The automotive industry is advancing in terms of the technologies proposed to improve people's commutes. However, motion sickness remains an unsolved issue that must be addressed to enable the full capabilities of these technologies. Within this context, predicting passenger MS is critical for developing human-centric technologies that can improve passenger comfort and productivity. While previous models for predicting MS have been proposed in the literature, the work presented here expands on predictive capabilities by leveraging new methods for physiological and data-driven models.

The first key contribution of this thesis was the development of a physiological visual-vestibular model capable of handling linear and angular motion data in three dimensions. A previously developed subjective vertical conflict vestibular model was expanded by including a human motion perception model to integrate visual stimuli with the goal of enabling accurate prediction of MS in the low-frequency range (<0.1Hz), addressing a key limitation of previously developed models. This model was validated for both motion simulator-based and on-road-based exposure. Furthermore, it demonstrated improved accuracy compared to the previous state-of-the-art physiological models, achieving higher agreement with the experimental dataset of Griffin et al. [94] and enabling improvements in predicted MS response when subjects performed cognitive tasks during on-road trials collected by Jones et

al. [2]. This represented a shift in the importance of considering visual stimuli when predicting motion sickness and opened a new realm of possibilities in terms of predictive modeling capabilities. Future work remains to characterize and quantify the visual flow for various conditions that might elicit different magnitudes of visual stimuli beyond the two conditions considered when the passenger was performing a task or not. In addition, future work remains on better characterizing model parameters, such as the rate of accumulation of MS scores, to accurately predict MS considering individual subject characteristics. This would enable higher prediction accuracy on an individual level, thereby improving the model's generalizability.

The second key contribution of this thesis was the development of data-driven frameworks for MS prediction using head motion data. A novel time-series feature engineering method for data-driven classification of MS using head motion data was proposed. This was the first end-to-end MS predictor using IMU data. In addition to the time-series methods for classification, this was the first study to propose the use of LSTM and NARX models for MS prediction. Further, it established a new benchmark for MS regression prediction by achieving an RMSE of 2.1. The time series dependency of MS with respect to head motion data was analyzed, indicating that self-reporting of MS can lag head motion exposure by more than 360 seconds. This characterization provides valuable insights into the mechanisms that lead to MS, such as characterizing the time delay between motion exposure and MS response. This insight can be applied not only to achieve a better understanding of MS but also to develop an array of technologies for on-road MS mitigation solutions. This work also proposed a framework for integrating subject demographics into MS prediction, which led to accuracy improvements of up to 7% per demographic variable considered and underscored the importance of using demographic descriptors as model inputs.

The third and final key contribution of this thesis was the application of multiple physiological data streams to predict MS with up to 81% binary classification accuracy. Through this work, it was possible to identify the optimal normalization techniques for physiologi-

cal data and to quantify the temporal dependencies of physiological data in terms of MS response. In addition, the relative comparison of the predictive importance of different physiological data streams was performed, providing insights into the most relevant sensors that must be used for MS prediction in the future. It was found that skin perspiration is the best physiological indicator of MS among the data streams considered, which corroborated the prior art. Further, it was found that sEMG data from the neck muscles can effectively predict MS, which is a new finding for the field. Finally, physiological markers were found to lead self-reported MS score by 180 seconds. This quantification allows researchers to better understand the temporal nature of MS symptoms and to apply this to future technology development. Fundamental limitations remain, as the physiological-based model performance was worse than IMU-based performance. This could be attributed to limitations with the currently available sensors for collecting physiological data or to potential room for improvement in model configuration. Based on these findings, using an IMU-based predictor is more beneficial than a physiological-based predictor. While this is promising in terms of real-world implementation, as head motion data is more easily accessible through non-intrusive methods, it highlights the potential for improving physiology-based prediction of MS using better physiological sensors and models.

While the proposed data-driven frameworks provide valuable contributions to the field, they also restate the need for an expanded dataset capturing human MS response. The field would largely benefit from the standardization of MS data collection processes and an integrated collaborative dataset that different researchers can leverage. Given the significant logistical burden of collecting MS data, collaboration across groups would enable the full capabilities of the proposed data-driven models.

Further, in this work, the data-driven models in Chapters 5 and 6 were not evaluated to differentiate the prediction performance between subjects included in the training set and subjects that have been exclusively used in the test set. Future work on characterizing the model performance for unseen subjects can improve the confidence in the generalizability of

the model for large-scale implementation. The expansion of subject demographics considered can also pave the way for higher generalizability by including subjects outside the recruitment criteria stipulated by the experimental study, such as age range.

Other individual predictive variables not explored as part of this work have the potential to improve model performance. For instance, subject state characteristics can be used to improve accuracy on the individual level by leveraging information such as hours of sleep, food intake, and stress level. In-cabin data, such as temperature, humidity and lighting, can be used to expand the variables of interest given that these have been demonstrated to correlate with MS response.

Given the inherit variability of self-reported MS scores, the model is subject to inconsistencies in human-based reporting. This can lead to inaccuracies in model performance, specially when considering inter-subject variability. Future work can expand on this by analyzing the variability in MS responses in the scale used by leveraging a larger dataset.

Another limitation of the data-driven work presented here is the realistic implementation of these models, considering the need for non-intrusive data acquisition approaches. Using non-intrusive occupant monitoring sensors would allow for the deployment of the models presented here. However, these non-intrusive sensors remain an ongoing problem in the automotive industry.

Future work remains to better characterize the impact of the features explicitly as a function of model performance to decrease the required computational time for the deployment of these models in edge and/or cloud compute applications. While the feature selection based on the Gini importance was sufficient to ensure accurate model performance without overly increasing dataset dimensionality, the analysis of their direct impact on model performance can enable optimization in terms of computational time.

In summary, the predictive models presented here are capable of predicting MS with a promising level of accuracy to achieve real-world applications. In the future, these models can be used to develop and evaluate technologies that can mitigate motion sickness for

passengers of on-road vehicles. Further, the findings obtained through the development of these models go beyond application and provide valuable insight into better understanding the fundamental aspects of motion sickness.

BIBLIOGRAPHY

[1] Barnaby E. Donohew and Michael J. Griffin. Motion sickness: effect of the frequency of lateral oscillation. *Aviation, Space, and Environmental Medicine*, 75(8):649–656, August 2004. Number: 8.

[2] Monica L. H. Jones, Victor C. Le, Sheila M. Ebert, Kathleen H. Sienko, Matthew P. Reed, and James R. Sayer. Motion sickness in passenger vehicles during test track operations. *Ergonomics*, 62(10):1357–1371, October 2019. Number: 10.

[3] MedlinePlus Genetics. Motion sickness. https://ghr.nlm.nih.gov/condition/motion-sickness, oct 29 2019. container-title: Genetics Home Reference.

[4] T. Fukuda. Postural Behaviour and Motion Sickness. *Acta Oto-Laryngologica*, 81(3-6):237–241, jan 1 1976.

[5] Julie Iskander, Mohammed Attia, Khaled Saleh, Darius Nahavandi, Ahmed Abobakr, Shady Mohamed, Houshyar Asadi, Abbas Khosravi, Chee Peng Lim, and Mohammed Hossny. From car sickness to autonomous car sickness: A review. *Transportation Research Part F: Traffic Psychology and Behaviour*, 62:716–726, 4 2019.

[6] Ouren X. Kuiper, Jelte E. Bos, Eike A. Schmidt, Cyriel Diels, and Stefan Wolter. Knowing What's Coming: Unpredictable Motion Causes More Motion Sickness. *Human Factors*, 62(8):1339–1348, 2020. _eprint: https://doi.org/10.1177/0018720819876139 PMID: 31590575.

[7] A. Rolnick and R. E. Lubow. Why is the driver rarely motion sick? The role of controllability in motion sickness. *Ergonomics*, 34(7):867–879, 7 1991. publisher-place: England PMID: 1915252.

[8] Monica L. H. Jones, Victor C. Le, Sheila M. Ebert, Kathleen H. Sienko, Matthew P. Reed, and James R. Sayer. Motion sickness in passenger vehicles during test track operations. *Ergonomics*, 62(10):1357–1371, 10 2019. PMID: 31282785.

[9] Zhaoxue Deng, Kun Yuan, and Xiang Xiao. Investigative examination of motion sickness indicators for electric vehicles. *Proceedings of the Institution of Mechanical Engineers, Part D: Journal of Automobile Engineering*, 0(0):09544070241251521, 0.

[10] Ouren X. Kuiper, Jelte E. Bos, Cyriel Diels, and Kia Cammaerts. Moving base driving simulators' potential for carsickness research. *Applied Ergonomics*, 81:102889, 11 2019.

[11] Panagiotis Matsangas, Michael E. McCauley, and William Becker. The Effect of Mild Motion Sickness and Sopite Syndrome on Multitasking Cognitive Performance. *Human Factors*, 56(6):1124–1135, sep 1 2014.

[12] Michael E. McCauley. Motion Sickness Incidence: Exploratory Studies of Habituation, Pitch and Roll, and the Refinement of a Mathematical Model. *Human Factors Research Inc., Santa Barbara Research Park, California, Technical Report 1733-2, Task No. NR 105-841, April 1976*, 1976. [Online; accessed 2020-08-26].

[13] J. F. O'Hanlon and M. E. McCauley. Motion sickness incidence as a function of the frequency and acceleration of vertical sinusoidal motion. *Aerospace Medicine*, 45(4):366–369, 4 1974. PMID: 4821729.

[14] Jelte E. Bos. Nuancing the relationship between motion sickness and postural stability. *Displays*, 32(4):189–193, October 2011. Number: 4.

[15] Nishant Jalgaonkar, Daniel Schulman, Adam Kim, Jiaxi Chen, and Shorya Awtar. Preemptive Haptic Stimuli to Mitigate Car Sickness and its Influence on Task Performance: A Pilot Study. In *2023 IEEE 26th International Conference on Intelligent Transportation Systems (ITSC)*, pages 5014–5019, September 2023. ISSN: 2153-0017.

[16] Min Deng, Aaron Gluck, Yijin Zhao, Da Li, Carol C. Menassa, Vineet R. Kamat, and Julian Brinkley. An analysis of physiological responses as indicators of driver takeover readiness in conditionally automated driving. *Accident Analysis & Prevention*, 195:107372, February 2024.

[17] J.E. Bos and W. Bles. Modelling motion sickness and subjective vertical mismatch detailed for vertical motions. *Brain Research Bulletin*, 47(5):537–542, November 1998. Number: 5.

[18] Wada, T., Kawano, J., Okafuji, Y., Takamatsu, A., and Mitsuhiro, M.,. A Computational Model of Motion Sickness Considering Visual and Vestibular Information. 2020.

[19] Norimasa Kamiji, Yoshinori Kurata, Takahiro Wada, and Shun'ichi Doi. Modeling and validation of carsickness mechanism. In *SICE Annual Conference 2007*, pages 1138–1143, September 2007.

[20] Shorya Awtar, Nishant M. JALGAONKAR, and Daniel Sousa SCHULMAN. Passenger State Modulation System For Passenger Vehicles Based On Prediction And Preemptive Control, April 2021. Inventors: _:n8161 Issue: US20210114553A1.

[21] Shorya Awtar. Deployment of a preemption based motion sickness prevention technology on a testbed vehicle in mcity. Technical report, University of Michigan. Transportation Research Institute, August 2023.

[22] Norimasa Kamiji, Yoshinori Kurata, Takahiro Wada, and Shun'ichi Doi. Modeling and validation of carsickness mechanism. In *SICE Annual Conference 2007*, pages 1138–1143, Takamatsu, Japan, September 2007. IEEE.

[23] Hassan Khalid, Osman Turan, and Jelte E. Bos. Theory of a subjective vertical–horizontal conflict physiological motion sickness model for contemporary ships. *Journal of Marine Science and Technology*, 16(2):214–225, June 2011. Number: 2.

[24] Charles M. Oman. A Heuristic Mathematical Model for the Dynamics of Sensory Conflict and Motion Sickness Hearing in Classical Musicians. *Acta Oto-Laryngologica*, 94(sup392):4–44, January 1982. Number: sup392.

[25] J T Reason. Motion Sickness Adaptation: A Neural Mismatch Model. *Journal of the Royal Society of Medicine*, 71(11):819–829, November 1978. Number: 11.

[26] Spencer Salter, Cyriel Diels, Paul Herriotts, Stratis Kanarachos, and Doug Thake. Model to predict motion sickness within autonomous vehicles. *Proceedings of the Institution of Mechanical Engineers, Part D: Journal of Automobile Engineering*, 234(5):1330–1345, April 2020. Number: 5.

[27] Robert Telban and Frank Cardullo. An integrated model of human motion perception with visual-vestibular interaction. In *AIAA Modeling and Simulation Technologies Conference and Exhibit*, Montreal,Canada, August 2001. American Institute of Aeronautics and Astronautics.

[28] Cyriel Diels and Peter A. Howarth. Frequency Characteristics of Visually Induced Motion Sickness. *Human Factors*, 55(3):595–604, June 2013. Number: 3 Publisher: SAGE Publications Inc.

[29] Henry Been-Lirn Duh, Donald E. Parker, James O. Philips, and Thomas A. Furness. "Conflicting" Motion Cues to the Visual and Vestibular Self- Motion Systems Around 0.06 Hz Evoke Simulator Sickness:. *Human Factors*, 8 2016. [Online; accessed 2020-08-26].

[30] Varun Kotian, Tugrul Irmak, Daan Pool, and Riender Happee. The role of vision in sensory integration models for predicting motion perception and sickness. *Experimental Brain Research*, 242(3):685–725, March 2024. Number: 3.

[31] Claudio Braccesi and Filippo Cianetti. Motion sickness. Part I: development of a model for predicting motion sickness incidence. *International Journal of Human Factors Modelling and Simulation*, 2:163–187, January 2011.

[32] Takahiro Wada, Junichiro Kawano, Yuki Okafuji, Atsushi Takamatsu, and Makita Mitsuhiro. *A Computational Model of Motion Sickness Considering Visual and Vestibular Information*. IEEE, October 2020.

[33] Ouren X. Kuiper, Jelte E. Bos, and Cyriel Diels. Looking forward: In-vehicle auxiliary display positioning affects carsickness. *Applied Ergonomics*, 68:169–175, 2018.

[34] Greg L Zacharias. *Motion Sensation Dependence on Visual and Vestibular Cues*. PhD thesis, Massachusetts Institute of Technology, 1977.

[35] Srikanth Kolachalama, Daniel Sousa Schulman, Bradley Kerr, Siyuan Yin, Michael Ben Wachsman, Jedidiah Ethan Shapiro Pienkny, Nishant M. Jalgaonkar, and Shorya Awtar. A deep learning framework for time series prediction of passenger motion sickness based on vehicle dynamics data. SAE Technical Paper 2025-01-8104, SAE International, Warrendale, PA, April 2025. Issue: 2025-01-8104 ISSN: 0148-7191, 2688-3627.

[36] Bin Ren, Wanli Guan, and Qinyu Zhou. Study of Motion Sickness Model Based on fNIRS Multiband Features during Car Rides. *Diagnostics*, 13(8):1462, January 2023. Number: 8 Publisher: Multidisciplinary Digital Publishing Institute.

[37] Sarah 'Atifah Saruchi, Mohd Hatta Mohammed Ariff, Hairi Zamzuri, Nurhaffizah Hassan, and Nurbaiti Wahid. Artificial neural network for modelling of the correlation between lateral acceleration and head movement in a motion sickness study. *IET Intelligent Transport Systems*, 13(2):340–346, February 2019. Number: 2.

[38] Nishant Jalgaonkar, Daniel Sousa Schulman, Ming Shao, Saharsh Jaisankar, Brandon Tarter, Nikitha MV, Jacqueline Buford, Sarah Chan, Michael Wachsman, and Shorya Awtar. Experimental investigation of the efficacy of preemptive tilting seats in mitigating carsickness. *Applied Ergonomics*, 125:104453, 2025.

[39] Daniel Sousa Schulman, Nishant Jalgaonkar, Sneha Ojha, Ana Rivero Valles, Monica L. H. Jones, and Shorya Awtar. A Visual-Vestibular Model to Predict Motion Sickness for Linear and Angular Motion. *Human Factors: The Journal of the Human Factors and Ergonomics Society*, page 00187208231200721, September 2023.

[40] Afsaneh Koohestani, Darius Nahavandi, Houshyar Asadi, Parham M. Kebria, Abbas Khosravi, Roohallah Alizadehsani, and Saeid Nahavandi. A Knowledge Discovery in Motion Sickness: A Comprehensive Literature Review. *IEEE Access*, 7:85755–85770, 2019.

[41] Eléonore H. Henry, Clément Bougard, Christophe Bourdin, and Lionel Bringoux. Car sickness in real driving conditions: Effect of lateral acceleration and predictability reflected by physiological changes. *Transportation Research Part F: Traffic Psychology and Behaviour*, 97:123–139, August 2023.

[42] Behrang Keshavarz, Katlyn Peck, Sia Rezaei, and Babak Taati. Detecting and predicting visually induced motion sickness with physiological measures in combination with machine learning techniques. *International Journal of Psychophysiology*, 176:14–26, June 2022.

[43] Ruichen Tan, Wenbo Li, Fengqing Hu, Xiaofeng Xiao, Shen Li, Yang Xing, Hong Wang, and Dongpu Cao. Motion Sickness Detection for Intelligent Vehicles: A Wearable-Device-Based Approach. In *2022 IEEE 25th International Conference on Intelligent Transportation Systems (ITSC)*, pages 4355–4362, October 2022.

[44] Jelte E. Bos and Willem Bles. Theoretical considerations on canal–otolith interaction and an observer model. *Biological Cybernetics*, 86(3):191–207, March 2002. Number: 3.

[45] Claremont, CA. The psychology of sea-sickness. *Psyche*, 11:86–90, 1931.

[46] J. Hill. The care of the sea-sick. *BMJ*, 2(3955):802–807, October 1936. Number: 3955.

[47] J. T. Reason and J. J. Brand. *Motion sickness*. Motion sickness. Academic Press, Oxford, England, 1975. Pages: vii, 310.

[48] Willem Bles, Jelte E Bos, Bernd de Graaf, Eric Groen, and Alexander H Wertheim. Motion sickness: only one provocative conflict? *Brain Research Bulletin*, 47(5):481–487, November 1998. Number: 5.

[49] Charles M. Oman. Sensory conflict in motion sickness: An observer theory approach. In *Pictorial communication in real and virtual environments*, July 1989.

[50] T. Fukuda. Postural Behaviour and Motion Sickness. *Acta Oto-Laryngologica*, 81(3-6):237–241, January 1976. Number: 3-6 Publisher: Taylor & Francis _eprint: https://doi.org/10.3109/00016487609119955.

[51] International Organization for Standardization. ISO 2631-1:1997, June 1997. Issue: ISO 2631-1:1997.

[52] A Graybiel, RS Kellogg, and RS Kennedy. Motion Sickness Symptomatology of Labyrinthine Defective and Normal Subjects During Zero Gravity Maneuvers. Technical report, U.S. Naval School of Aviation Medicine, 1964.

[53] J. T. Reason. Relations Between Motion Sickness Susceptibility, the Spiral After-Effect and Loudness Estimation. *British Journal of Psychology*, 59(4):385–393, 1968. Number: 4 _eprint: https://onlinelibrary.wiley.com/doi/pdf/10.1111/j.2044-8295.1968.tb01153.x.

[54] A. J. C. Reuten, S. A. E. Nooij, J. E. Bos, and J. B. J. Smeets. How feelings of unpleasantness develop during the progression of motion sickness symptoms. *Experimental Brain Research*, 239(12):3615–3624, December 2021. Number: 12.

[55] Michael E. McCauley, Jackson W. Royal, C. Dennis Wylie, James F. O'Hanlon, and Robert R. Mackie. Motion Sickness Incidence: Exploratory Studies of Habituation, Pitch and Roll, and the Refinement of a Mathematical Model:. Technical report, Defense Technical Information Center, Fort Belvoir, VA, April 1976.

[56] Bunji Atsumi, Haruhisa Tokunaga, Hitoshi Kanamori, Tomoko Sugawara, Eiichi Yasuda, and Hajime Inagaki. Evaluation of vehicle motion sickness due to vehicle vibration. *JSAE Review*, 23(3):341–346, July 2002. Number: 3.

[57] Takahiro Wada. Computational Model of Motion Sickness Describing the Effects of Learning Exogenous Motion Dynamics. *Frontiers in Systems Neuroscience*, 15, 2021.

[58] Shota Inoue, Hailong LIU, and Takahiro Wada. Revisiting motion sickness models based on SVC theory considering motion perception. Technical Report 0148-7191, SAE Technical Paper, 2023.

[59] Jelte E. Bos, Willem Bles, and Eric L. Groen. A theory on visually induced motion sickness. *Displays*, 29(2):47–57, March 2008. Number: 2.

[60] Jeong Hun Hong, Jin Sung Kim, Ying Shuai Quan, Taewoong Park, Chang Seop An, and Chung Choo Chung. Adaptive Cruise Control with Motion Sickness Reduction: Data-driven Human Model and Model Predictive Control Approach. In *2022 IEEE 25th International Conference on Intelligent Transportation Systems (ITSC)*, pages 1464–1470, Macau, China, October 2022. IEEE.

[61] Ji-Seon Bang, Dong-Ok Won, Tae-Eui Kam, and Seong-Whan Lee. Motion Sickness Prediction Based on Dry EEG in Real Driving Environment. *IEEE Transactions on Intelligent Transportation Systems*, 24(5):5442–5455, May 2023. Number: 5 Conference Name: IEEE Transactions on Intelligent Transportation Systems.

[62] Bin Ren and Qinyu Zhou. Assessing Passengers' Motion Sickness Levels Based on Cerebral Blood Oxygen Signals and Simulation of Actual Ride Sensation. *Diagnostics*, 13(8):1403, January 2023. Number: 8 Publisher: Multidisciplinary Digital Publishing Institute.

[63] Ananth N. Ramaseri-Chandra, Hassan Reza, and Prasad Pothana. Exploring the feasibility of head-tracking data for cybersickness prediction in virtual reality. *Electronics*, 14(3), 2025.

[64] Masoud Salehi, Nikoo Javadpour, Brietta Beisner, Mohammadamin Sanaei, and Stephen B. Gilbert. Cybersickness detection through head movement patterns: A promising approach. In *Artificial Intelligence in HCI: 5th International Conference, AI-HCI 2024, Held as Part of the 26th HCI International Conference, HCII 2024, Washington, DC, USA, June 29–July 4, 2024, Proceedings, Part II*, page 239–254, Berlin, Heidelberg, 2024. Springer-Verlag.

[65] Chengcheng Hua, Lining Chai, Ying Yan, Jia Liu, Qiaoxiu Wang, Rongrong Fu, and Zhanfeng Zhou. Assessment of Virtual Reality Motion Sickness Severity Based on EEG via LSTM/BiLSTM. *IEEE Sensors Journal*, 23(20):24839–24848, October 2023. Number: 20 Conference Name: IEEE Sensors Journal.

[66] Marco Recenti, Carlo Ricciardi, Romain Aubonnet, Ilaria Picone, Deborah Jacob, Halldór Á R. Svansson, Sólveig Agnarsdóttir, Gunnar H. Karlsson, Valdís Baeringsdóttir, Hannes Petersen, and Paolo Gargiulo. Toward Predicting Motion Sickness Using Virtual Reality and a Moving Platform Assessing Brain, Muscles, and Heart Signals. *Frontiers in Bioengineering and Biotechnology*, 9, April 2021. Publisher: Frontiers.

[67] Yan Li, Aie Liu, and Li Ding. Machine learning assessment of visually induced motion sickness levels based on multiple biosignals. *Biomedical Signal Processing and Control*, 49:202–211, March 2019.

[68] Tae Min Lee, Jong-Chul Yoon, and In-Kwon Lee. Motion Sickness Prediction in Stereoscopic Videos using 3D Convolutional Neural Networks. *IEEE Transactions on Visualization and Computer Graphics*, 25(5):1919–1927, May 2019. Number: 5 Conference Name: IEEE Transactions on Visualization and Computer Graphics.

[69] Nitish Padmanaban, Timon Ruban, Vincent Sitzmann, Anthony M. Norcia, and Gordon Wetzstein. Towards a Machine-Learning Approach for Sickness Prediction in 360° Stereoscopic Videos. *IEEE Transactions on Visualization and Computer Graphics*, 24(4):1594–1603, April 2018. Number: 4.

[70] Jinwoo Kim, Heeseok Oh, Woojae Kim, Seonghwa Choi, Wookho Son, and Sanghoon Lee. A Deep Motion Sickness Predictor Induced by Visual Stimuli in Virtual Reality. *IEEE Transactions on Neural Networks and Learning Systems*, 33(2):554–566, February 2022. Number: 2 Conference Name: IEEE Transactions on Neural Networks and Learning Systems.

[71] Chin-Teng Lin, Shu-Fang Tsai, Hua-Chin Lee, Hui-Lin Huang, Shinn-Ying Ho, and Li-Wei Ko. Motion sickness estimation system. In *The 2012 International Joint Conference on Neural Networks (IJCNN)*, pages 1–6, June 2012. ISSN: 2161-4407.

[72] Chung-Yen Liao, Shao-Kuo Tai, Rung-Ching Chen, and Hendry Hendry. Using EEG and Deep Learning to Predict Motion Sickness Under Wearing a Virtual Reality Device. *IEEE Access*, 8:126784–126796, 2020. Conference Name: IEEE Access.

[73] Leo Breiman, Jerome H. Friedman, Richard A. Olshen, and Charles J. Stone. *Classification And Regression Trees*. Routledge, October 2017.

[74] Benyamin Ghojogh, Mark Crowley, Fakhri Karray, and Ali Ghodsi. *Elements of Dimensionality Reduction and Manifold Learning*. Springer International Publishing, 2023.

[75] Nishant Jalgaonkar, Daniel Sousa Schulman, Sneha Ojha, and Shorya Awtar. A Visual-Vestibular Model to Predict Motion Sickness Response in Passengers of Autonomous Vehicles. *SAE International Journal of Advances and Current Practices in Mobility*, 3(5):2421–2432, 4 2021.

[76] T. Haslwanter, R. Jaeger, S. Mayr, and M. Fetter. Three-dimensional eye-movement responses to off-vertical axis rotations in humans. *Experimental Brain Research*, 134(1):96–106, August 2000. Number: 1.

[77] Jelte E. Bos. Less sickness with more motion and/or mental distraction. *Journal of Vestibular Research*, 25(1):23–33, March 2015. Number: 1.

[78] Nathan C. Sepich, Angelica Jasper, Stephen Fieffer, Stephen B. Gilbert, Michael C. Dorneich, and Jonathan W. Kelly. The impact of task workload on cybersickness. *Frontiers in Virtual Reality*, 3, 2022.

[79] Panagiotis Matsangas, Michael E. McCauley, and William Becker. The Effect of Mild Motion Sickness and Sopite Syndrome on Multitasking Cognitive Performance. *Human Factors*, 56(6):1124–1135, September 2014. Number: 6 Publisher: SAGE Publications Inc.

[80] Anna Sjörs Dahlman, Joakim Dahlman, Pontus Lundgren, and Björn Gerdle. Effects of Motion Sickness on Encoding and Retrieval Performance and on Psychophysiological Responses. *Journal of Ergonomics*, 04, 1 2014.

[81] Monica Lynn Haumann Jones, Sheila Ebert, and Matthew Reed. Sensations Associated with Motion Sickness Response during Passenger Vehicle Operations on a Test Track. *SAE International Journal of Advances and Current Practices in Mobility*, 1(4):1398–1403, April 2019. Number: 4.

[82] Norimasa Kamiji, Yoshinori Kurata, Takahiro Wada, and Shun'ichi Doi. Modeling and validation of carsickness mechanism. In *SICE Annual Conference 2007*, pages 1138–1143, 9 2007.

[83] Nishant Jalgaonkar, Daniel Sousa Schulman, Kexin Huang, Yung-Chun Lin, Cynthia Monickaraj, Haocheng Ren, Shutian Wu, Zhihao Zhang, Aditya Kore, Nick Farid, and Shorya Awtar. Efficacy of preemptive haptic stimuli in mitigating carsickness in passengers performing tasks. *In Review*, 2025.

[84] Srikanth Kolachalama and Hafiz Malik. Extended Deep Learning Model to Predict the Electric Vehicle Motor Operating Point. SAE Technical Paper 2024-01-2551, SAE International, Warrendale, PA, April 2024. Issue: 2024-01-2551 ISSN: 0148-7191, 2688-3627.

[85] Srikanth Kolachalama and Sridhar Lakshmanan. Using Deep Learning to Predict the Engine Operating Point in Real-Time. SAE Technical Paper 2021-01-0186, SAE International, Warrendale, PA, April 2021. Issue: 2021-01-0186 ISSN: 0148-7191, 2688-3627.

[86] Srikanth Kolachalama and Hafiz Malik. Neural Network Model to Predict the Thermal Operating Point of an Electric Vehicle. SAE Technical Paper 2023-01-0134, SAE International, Warrendale, PA, April 2023. Issue: 2023-01-0134 ISSN: 0148-7191, 2688-3627.

[87] Saba Ale Ebrahim, Javad Poshtan, Seyedh Mahboobeh Jamali, and Nader Ale Ebrahim. Quantitative and Qualitative Analysis of Time-Series Classification Using Deep Learning. *IEEE Access*, 8:90202–90215, 2020. Conference Name: IEEE Access.

[88] Mohamed Elgendi, Ian Norton, Matt Brearley, Derek Abbott, and Dale Schuurmans. Systolic peak detection in acceleration photoplethysmograms measured from emergency responders in tropical conditions. *PLoS ONE*, 8(10):e76585, October 2013.

[89] Alberto Greco, Gaetano Valenza, Antonio Lanata, Enzo Pasquale Scilingo, and Luca Citi. cvxeda: A convex optimization approach to electrodermal activity processing. *IEEE Transactions on Biomedical Engineering*, 63(4):797–804, 2016.

[90] Lin Li, Jian Hui Wang, and Shuai Ban. A design method for iir and fir digital notch filter used to semg. In *Information Technology Applications in Industry*, volume 263 of *Applied Mechanics and Materials*, pages 184–187. Trans Tech Publications Ltd, 2 2013.

[91] Diana C. Toledo-Pérez, Juvenal Rodríguez-Reséndiz, Roberto A. Gómez-Loenzo, and J. C. Jauregui-Correa. Support vector machine-based emg signal classification techniques: A review. *Applied Sciences*, 9(20), 2019.

[92] Dominique Makowski, Tam Pham, Zen J. Lau, Jan C. Brammer, François Lespinasse, Hung Pham, Christopher Schölzel, and S. H. Annabel Chen. NeuroKit2: A python toolbox for neurophysiological signal processing. *Behavior Research Methods*, 53(4):1689–1696, feb 2021.

[93] Ruimin Gao and Monica Jones. Signal quality assessment algorithm for photoplethysmogram data using wrist motion data. *In Review*, 2025.

[94] Barnaby E. Donohew and Michael J. Griffin. Motion sickness: effect of the frequency of lateral oscillation. *Aviation, space, and environmental medicine*, 75(8):649–656, 8 2004. publisher-place: United States PMID: 15328780.